

Review

# Two-Dimensional Non-Carbon Materials-Based Electrochemical Printed Sensors: An Updated Review

Shaili Falina <sup>1,2</sup>, Khairu Anuar <sup>1</sup>, Saiful Arifin Shafiee <sup>3</sup>, Joon Ching Juan <sup>4</sup>, Asrulnizam Abd Manaf <sup>1,\*</sup>, Hiroshi Kawarada <sup>2,5</sup> and Mohd Syamsul <sup>2,6,\*</sup>

<sup>1</sup> Collaborative Microelectronic Design Excellence Center (CEDEC), Universiti Sains Malaysia, Sains@USM, Bayan Lepas 11900, Pulau Pinang, Malaysia

<sup>2</sup> Faculty of Science and Engineering, Waseda University, Tokyo 169-8555, Japan

<sup>3</sup> Department of Chemistry, Kulliyah of Science, International Islamic University Malaysia, Bandar Indera Mahkota, Kuantan 25200, Pahang, Malaysia

<sup>4</sup> Nanotechnology & Catalyst Research Centre (NANOCAT), Institute of Postgraduate Studies, University Malaya, Kuala Lumpur 50603, Malaysia

<sup>5</sup> The Kagami Memorial Laboratory for Materials Science and Technology, Waseda University, 2-8-26 Nishiwaseda, Shinjuku, Tokyo 169-0051, Japan

<sup>6</sup> Institute of Nano Optoelectronics Research and Technology (INOR), Universiti Sains Malaysia, Sains@USM, Bayan Lepas 11900, Pulau Pinang, Malaysia

\* Correspondence: eearulnizam@usm.my (A.A.M.); nasyriq@usm.my (M.S.)

**Abstract:** Recently, there has been increasing interest in electrochemical printed sensors for a wide range of applications such as biomedical, pharmaceutical, food safety, and environmental fields. A major challenge is to obtain selective, sensitive, and reliable sensing platforms that can meet the stringent performance requirements of these application areas. Two-dimensional (2D) nanomaterials advances have accelerated the performance of electrochemical sensors towards more practical approaches. This review discusses the recent development of electrochemical printed sensors, with emphasis on the integration of non-carbon 2D materials as sensing platforms. A brief introduction to printed electrochemical sensors and electrochemical technique analysis are presented in the first section of this review. Subsequently, sensor surface functionalization and modification techniques including drop-casting, electrodeposition, and printing of functional ink are discussed. In the next section, we review recent insights into novel fabrication methodologies, electrochemical techniques, and sensors' performances of the most used transition metal dichalcogenides materials (such as MoS<sub>2</sub>, MoSe<sub>2</sub>, and WS<sub>2</sub>), MXenes, and hexagonal boron-nitride (hBN). Finally, the challenges that are faced by electrochemical printed sensors are highlighted in the conclusion. This review is not only useful to provide insights for researchers that are currently working in the related area, but also instructive to the ones new to this field.

**Keywords:** 2D materials; non-carbon; electrochemical; screen printed electrode; sensors; TMDCs; MXenes; hexagonal boron-nitride



**Citation:** Falina, S.; Anuar, K.; Shafiee, S.A.; Juan, J.C.; Manaf, A.A.; Kawarada, H.; Syamsul, M. Two-Dimensional Non-Carbon Materials-Based Electrochemical Printed Sensors: An Updated Review. *Sensors* **2022**, *22*, 9358. <https://doi.org/10.3390/s22239358>

Academic Editor: Dmitry K. Polyushkin

Received: 31 October 2022

Accepted: 22 November 2022

Published: 1 December 2022

**Publisher's Note:** MDPI stays neutral with regard to jurisdictional claims in published maps and institutional affiliations.



**Copyright:** © 2022 by the authors. Licensee MDPI, Basel, Switzerland. This article is an open access article distributed under the terms and conditions of the Creative Commons Attribution (CC BY) license (<https://creativecommons.org/licenses/by/4.0/>).

## 1. Introduction

Electrochemical sensors have been widely used to detect various analytes of interest and display high sensitivity and selectivity, especially when combined with the use of two-dimensional nanomaterials with highly catalytic properties. The advancement in miniaturization and microfabrication of electrochemical sensors has led to renewed interest in the development of disposable electrodes as an analytical power tool. The application of disposable electrodes as point-of-care diagnostics and in situ analytical monitoring devices in biomedical, pharmaceutical [1], industrial [2], food safety [3], and environmental fields [4] has been the major focus of research in this field. Printing electrodes is currently the most popular method for fabricating disposable sensors. It is a fast and rapid method

to produce sensors in mass volume. Additionally, it is also low-cost, as its fabrication calls for the use of different cheap substrates such as ceramics, paper, or plastics [5–7]. The electrodes can be printed with carbon or graphite ink, which is also economical compared to the fabrication of traditional electrochemical sensors.

Printed electronics have emerged as a current groundbreaking technology in electrochemical sensor fabrication, mainly due to advances in printable metallic, insulating, and semiconductor materials as well as mature printing techniques. In the early stages, printed electronics were focused on the display and lighting industries [8,9]. However, as time goes on, the printed electronic industries have broadened towards electronic devices [10–12], sensors [13–15], and circuits [16–18]. To date, various printing techniques have been introduced and developed, including screen-printing, off-set printing, gravure printing, spray coating, ink-jet printing, and many other hybrid printing techniques. Among these techniques, screen-printing and inkjet-printing are the popular choices to fabricate printed sensors. Standard sensor fabrication employs blankets of material deposition, photolithography, and etching procedures that are not only complicated, but also expensive and wasteful. Contrastingly, for the sensor that is fabricated through the printing method, only minimal and selective material deposition is required. Cost efficiency, high volume, and roll-to-roll manufacturing are major strengths of printed sensors. Beyond that, it also allows for the capability of printing sensor devices on soft, flexible, thin, and unconventional substrates, which enables wearable sensor applications. Healthcare is currently the biggest application field for printed sensors. To date, printed sensors have been widely studied as wearable and point-of-care (PoC) diagnostic tools.

Generally, printable electrochemical sensors can be categorized into two groups: (1) contact printing, which includes gravure, flexographic, off-set printing, and screen-printing, and (2) non-contact printing comprising inkjet printing, aerosol jet printing, laser-induced forward transfer (LIFT), micro and nano-pen printing [19–22]. The contact printing generally employs a mask-based printing technique in which a particular pattern is inked onto a substrate through a mask. In this technique, the substrate and mask are in physical contact. On the other hand, non-contact printing is a maskless printing technique in which the ink is dispensed through openings or nozzles. The sensor structure is defined by moving the stage in a pre-programmed pattern. In contrast to contact printing, non-contact printing has benefits in terms of reduced material waste, ameliorated resolution, enabling miniaturization, and complex pattern printing. Figure 1 below illustrates the printing techniques that are commonly used to fabricate electrochemical sensors.

At present, a vast body of literature has been published on 2D materials for sensing applications. Graphene and the other carbon materials (graphene oxide, graphene reduced oxides, carbon nanotubes, etc.) have attracted significant attention from academic and commercial researchers owing to their exceptional properties, such as biocompatibility, adjustable surface properties, fast electron transfer capability, and large surface area [23–26]. Nevertheless, the families of 2D non-carbon materials have also shown rapid advancement along with the 2D carbon materials. Most of the non-carbon materials share similar properties with those of carbon materials. However, the non-carbon materials certainly have advantages over the carbon materials in some areas. For example, MXenes and  $\text{MoS}_2$  have been in the spotlight for electrochemical sensing applications due to their tunable bandgap property [27,28], which help enhance sensing performance by reducing the signal-to-noise ratio. The non-carbon materials also offer an extensive range of materials compared to carbon materials. Up to date, about 40 different TMDC compounds exist with astonishing properties and the possibility of interconversion to various nano-dimensions such as 0-dimension (0D), 1-dimension (1D), and 2-dimension (2D) structures [29]. Although hexagonal boron nitride (hBN) materials are not very popular as sensing materials due to their insulation property, they are a very useful material for reinforcement of polymeric films [30]. While these non-carbon materials demonstrate that they exceed the merits of the carbon families, several drawbacks also have been identified. MXenes have poor mechanical property, easy restacking (aggregation), and relatively small lateral size, as

well as poor stability in oxygen atmosphere, thereby restricting its application for highly durable and flexible wearable sensors [31]. When compared to graphene, TMDC materials have relatively low carrier mobility ( $200 \text{ cm}^2 \text{ V}^{-1} \text{ s}^{-1}$  in the case of  $\text{MoS}_2$ , in contrast to graphene, where its carrier mobility can be up to  $200,000 \text{ cm}^2 \text{ V}^{-1} \text{ s}^{-1}$ ) [32]. In principle, the hBN surface is a molecularly smooth basal plane without any functionalities. To be able to operate as a sensing material, surface modification is usually essential in the sensor fabrication step. It has been reported that modification and functionalization on the hBN surface was quite a challenge, attributed to its dense structure [33].

This review aims to provide an overview of recent studies in the development of non-carbon two-dimensional (2D) materials on printed electrochemical sensors over the past five years (from 2018 to present). During this period, many review articles have been published in the field of printed sensors and 2D materials. It may, however, be noted that most of the review articles were focused on the advancements in 2D materials on electrochemical sensors in general [34–40]. Herein, we narrow down the scope of our studies to advance electrochemical printed sensor integration with non-carbon 2D materials as sensing platforms. We present our materials in three main sections covering transitional metal-dichalcogenides (TMDCs), MXenes, and hexagonal boron-nitrides (hBN). Particular emphasis has been given to the most common TMDCs materials, including molybdenum disulfides ( $\text{MoS}_2$ ), molybdenum diselenides ( $\text{MoSe}_2$ ), and tungsten disulfides ( $\text{WS}_2$ ). We cover innovative breakthroughs and applications of these 2D materials in the development of next generation printed electrochemical sensors. Although it should be borne in mind that this review is restricted to printed electrochemical sensors for biomolecule detection (biosensor), pharmaceutical, food safety, and environmental monitoring. Humidity and gas printed electrochemical sensors are excluded from this review as they have recently been comprehensively reviewed elsewhere [41–44]. Beyond that, this review also presents the principle and operation of printed sensors, electrochemical technique analysis, as well as surface modification and functionalization specifically on printed electrochemical sensors in the first part of the article. This review is intended to give an update on recent advances, key developments, and applications. The authors sincerely apologize for any possible oversight of other key papers in this field.

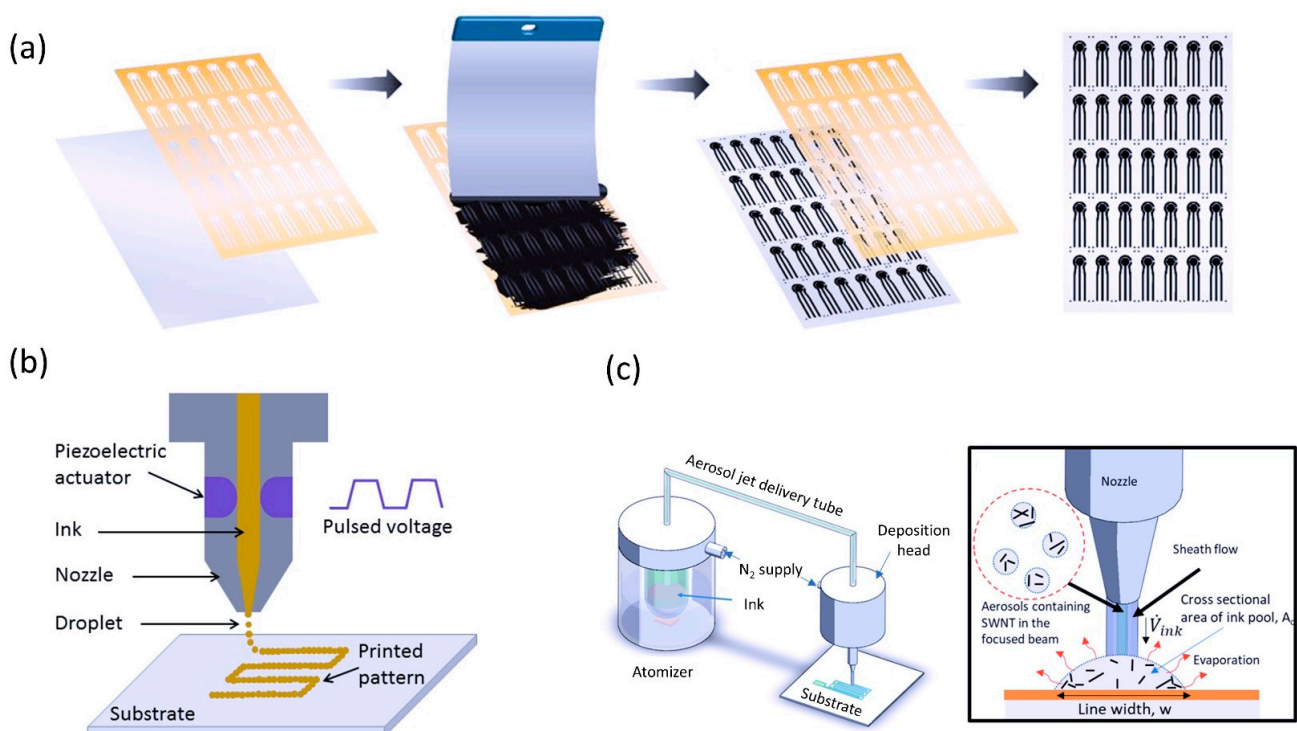


**Figure 1.** Printed sensor fabrication techniques (a) Screen-printing. Reproduced with permission from [45].

Copyright 2018 Plos ONE. (b) Ink-jet printing. Reproduced with permission from [46]. Copyright 2018 IOP Publishing All rights reserved. (c) Aerosol jet printing and its zoomed-in schematic of aerosol jet deposition. Reprinted (adapted) with permission from [47]. Copyright 2019 American Chemical Society.

## 2. Printed Electrochemical Sensors and Electrochemical Technique Analysis

The fabrication of printed electrochemical sensors frequently follows similar ideas to those of standard electrochemical electrodes in terms of structure. Generally, it is fabricated as a three-electrode system, which encompasses a working electrode (WE), a reference electrode (RE), and a counter electrode (CE). The electrode components are constructed by printing different inks in successive layers to create a final product. The printed electrodes often require curing procedures before use to anneal the layer of ink together with the substrate underneath for better stability [48]. The WE and CE are usually printed with the same conductive ink material, while the RE is usually printed with silver/silver chloride (Ag/AgCl) conductive ink, to replicate the reference Ag/AgCl electrode in the standard electrochemical set-up. The electrochemical sensor performance corresponds to a few factors, including structure, loading mass, specific areas, mechanical property, and ink formulation of the printable electrodes. Therefore, it is important to choose high performance electrode materials and ink formulations with exceptional rheological properties. For WE and CE, carbon and graphite inks are two common inks that have widely been used as printable electrode sensors owing to their electrically conductive properties and capability to electrocatalyze many oxidation/reduction processes [49,50]. A number of studies have employed silver tracks underneath the carbon or graphite printed electrodes to improve the electrode's conductivity [51–53]. Thanks to their high conductivity, gold, silver, and platinum material inks also make good printable electrodes for sensor applications. However, due to their higher cost, these inks are less popular choices compared to carbon and graphite ink. As regards gold ink, the generation of self-assembled monolayers (SAM) on gold surface through a strong Au-S bond has attracted many researchers to employ gold ink in screen-printed electrode (SPE) fabrication [54]. Besides electrode ink material, another important component in printed sensor fabrication is the substrate designer's intended application purposes. For example, for health monitoring applications, the sensor electrode is usually printed on tattoo transfer paper or directly stamped on the electrodes on the skin's epidermis. Some of the health monitoring sensors are printed on textiles. These sensors are customarily known as wearable sensors. For other applications, sensor electrodes can also be printed on thin-film plastic. Polyethylene terephthalate (PET), polyethylene naphthalate (PEN), and polyimide (PI) are the thin-film plastics that are frequently used for printing electrode sensors. However, it should be noted that these substrates must withstand heat transfer during the annealing process. Figure 2a,b show the three-electrode system of printed electrochemical sensors and printed electrochemical sensors on various types of substrates, respectively.

Next, we outline electrochemical sensing techniques such as amperometric, impedimetric, potentiometric, and voltammetric sensing. A detailed discussion of these electrochemical techniques has been excellently reviewed by Sardini et al. [59]. Nevertheless, we would like to lay out a short overview and conception to readers about analysis techniques that are usually used for electrochemical printed sensors.

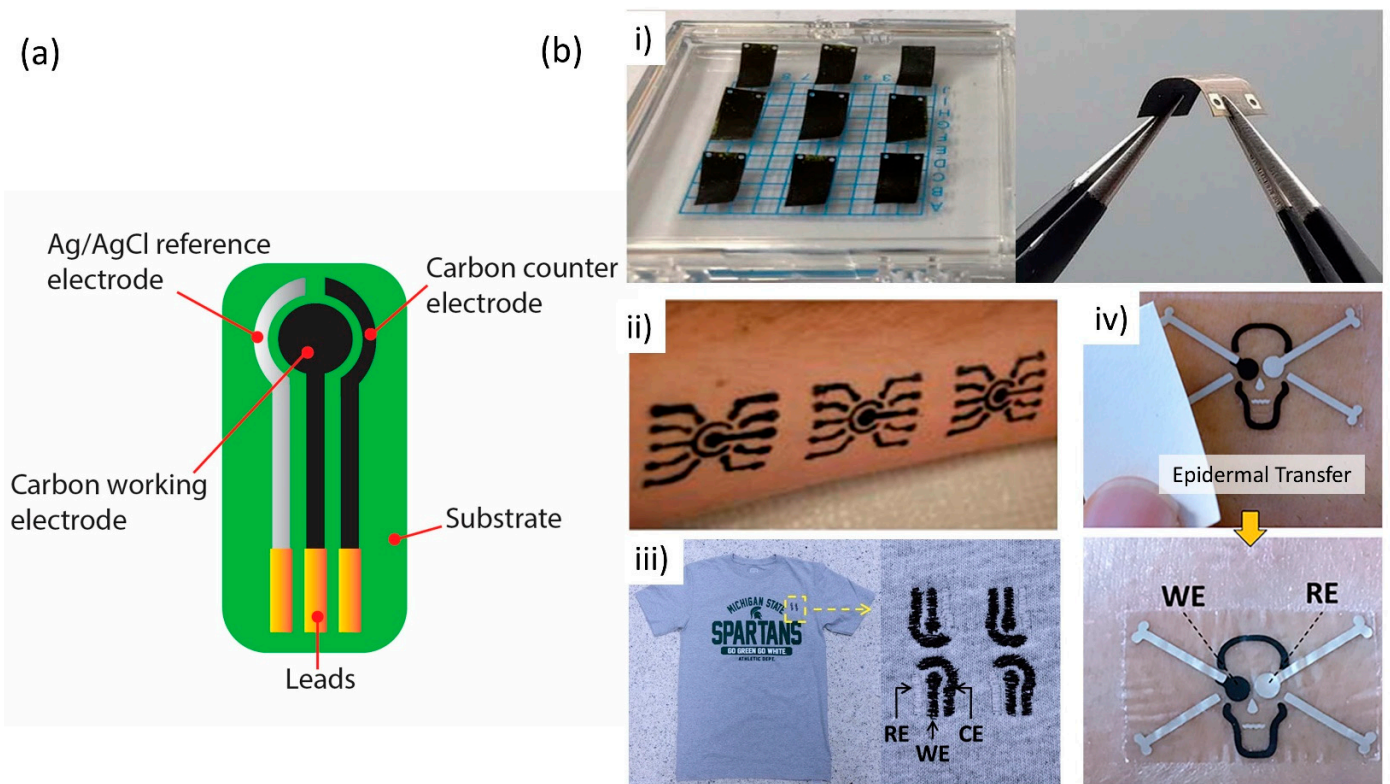


**Figure 2.** (a) A scheme of construction for a printed electrochemical sensor. The printed electrochemical sensors consist of three electrode systems, the working electrode, the counter electrode, and the reference electrode. (b) Printed sensor electrodes on various types of substrates, (b-i) printed electrochemical pH sensor on a flexible thin film. Reproduced/Adapted from Ref. [55] with permission from The Royal Society of Chemistry, (b-ii) sensor arrays printed on the skin epidermis. Reproduced/Adapted from Ref. [56] with permission from The Royal Society of Chemistry, (b-iii) printed sensors on textile and its zoomed-in image. Reproduced/Adapted from Ref. [57] with permission from The Royal Society of Chemistry, and (b-iv) printed chemical sensor on tattoo transfer paper. Reprinted with permission from [58]. Copyright 2018 Elsevier.

- (1) Amperometric—Amperometric techniques measure the resultant current from oxidation and reduction activities of an electroactive species, exchanging electrons with WE conductive surface, where this current is measured at a constant voltage. The advantage of this particular analysis technique is that it allows for highly sensitive and rapid analysis. Despite its convenience, this analysis technique tends to suffer from cross-sensitivity, interferences with buffer composition, and the effects of surrounding solution [60]. Chronoamperometry is the advanced version of the amperometry technique. A steady current is measured as a function of time, when a controlled potential technique with a stepwise profile is applied at the working electrode. In this case, the reduction and expansion of diffusion layer at the electrode surface cause the alternation in current. This type of analysis can be used to measure current–time dependence for the electroactive species activity occurring at the WE.
- (2) Impedimetric—Electrochemical impedance spectroscopy (EIS) has received significant interest from researchers for sensor analysis, particularly in biosensors due to its advantage where only a low voltage is required, which does not destroy or interrupt the bio-recognition layers on WE [61]. EIS measures the direct correlation of impedance changes with changes of target analyte concentration. Concisely, the biomolecules bound onto the printed electrode act as an insulator. A small alternate voltage is applied to WE and CE with a constant amplitude (typically from 5 mV to 10 mV) and a defined frequency range (usually from 100 kHz to 1 mHz), resulting

in an alternate current response. EIS data are commonly accompanied by Nyquist plot ( $Z_{\text{imag}}$  against  $Z_{\text{real}}$ ). The data collected with EIS can be modeled with appropriate equivalent electrical circuit according to the electrochemical events occurring in the sample. The parameter's values are adjusted until the mathematical function is comparable to the experimental data within a certain margin of error.

- (3) Potentiometric—Potentiometric analysis technique is performed at zero-current conditions to measure the accumulation of charge potential at WE compared to RE in an electrochemical activity. The potential of WE depends on the concentration of the analyte (accumulation of charges will proportionally decrease or increase the potential of WE depending on the electrode surface), while the RE is essential to provide a potential reference.
- (4) Voltammetric—Cyclic voltammetry (CV) is an overwhelmingly popular technique to obtain information of redox potential and electrochemical rates of the analyte. In this technique, a series of voltages are applied to the sensor electrode, and the resulting current is measured. The CV technique is often carried out in a partial cycle, one full cycle, or a series of cycles to study redox processes and monitor reaction intermediates as well as reaction product stability. Aside from CV, differential pulse voltammetry (DPV) also falls in the class of voltammetric techniques. Unlike CV, DPV measures the current immediately before each potential change. Therefore, the DPV graph represents current variation as a function of potential. Another major voltammetric technique that is often found in literature is square-wave voltammetry (SWV). SWV is an analysis technique that superimposes a high amplitude, high frequency square-wave signal onto a fast staircase waveform as the input, where the output is response current measured in forward pulse and reverse pulse. SWV is usually employed to study the mechanism, kinetics, and thermodynamics of a chemical reaction. One distinct advantage of SWV analysis is that it offers a very sensitive direct analysis down to parts per trillion (ppt) level [62].
- (5) Chronocoulometry—Chronocoulometry analysis is performed to quantify cumulative charge ( $Q$ ) that passes through electrochemistry electrode as a function of time. This analysis technique is established based on Faraday's first and second laws of electroanalysis [63], where (1) the amount of deposited material on the electrode surface (during electrolysis) is directly proportionate to the quantity of electricity ( $Q$ ) that passes through the electrolyte, and (2) the mass of ions deposited on the electrode are equivalent mass with the substance electrolyzed. When a single or double pulse of potential is applied to the electrochemistry electrode, the resulting charge accumulation curve vs. time response can be obtained. Chronocoulometry has the same input potential as the chronoamperometry analysis; however, they provide different output results. Chronocoulometry output is the charge ( $Q$ ), whereas chronoamperometry output is the current ( $I$ ).

### 3. Surface Modification and Functionalization of Printed Sensors

To function as a sensor, the printed working electrode (sensing area) often requires modification with a layer of nanomaterials to enhance the electrochemical response towards the anticipated target analyte. Some of the sensors, specifically printed biosensors, call for functionalization of their WE with bio-species such as antibodies, enzymes, aptamers, and DNA as their sensing probes to capture the desired target. The three most common strategies for integrating a modifier and the sensing probe onto the printed working electrode are the drop-casting technique, electrodeposition, and ink formulation for direct printing. It is vital to ensure that the modifier is firmly attached to the working electrode and will not be dissolved in the surrounding solution. The attached sensing elements on the electrode are the determining factor for the performance of a reliable sensor. Drop-casting is an overwhelmingly popular approach for the preparation of printed sensors' electrodes. In this approach, a drop of liquid containing suspension of material of interest is drop-cast on the sensing electrode as in Figure 3a, ideally confined to the electrode without overspill

outside the electrode surface area. Typically, for surface modification with nanomaterial using the drop-casting method, the electrode surface is left to dry before use. Recently, Kumar and colleagues wrote an excellent review of drop-casting technique reliability from an experimental perspective [64]. The review provides an in-depth understanding of drop-casting challenges and to what extent they can result in a reproducible surface. The authors discussed the main concern associated with the drop-casting technique, which is coffee ring and its related effect. Coffee ring effect is a ring-like pattern that generally occurs when the sessile droplet containing suspended particle is evaporated in ambient conditions. Deegan et al. [65] thoroughly observed and examined the liquid's behavior upon drying, which he interpreted in respect of the coffee stain. According to Deegan, taking a spilled drop of coffee as an example, at first the coffee particles are dispersed over the entire drop and slowly become concentrated at the periphery, in contrast to the center of the stain. Notably, the coffee ring results in a disruption of uniform material particle distribution [66–68] and therefore generates a suboptimal electrochemical response. Because of uncontrollable particle distribution, a sensor that utilizes the drop-casting technique for surface modification is rather difficult to reproduce. Kumar et al. also highlighted the efforts that have been made to mitigate the coffee ring effect, such as (1) choosing super hydrophobic surfaces can help to suppress the coffee ring effect by inducing the inward circulatory flow of the solute particles, resulting in more homogeneous deposition, (2) utilizing electrowetting method, which helps make the deposited solute particles mobile and not static, (3) modifying the shape of solute particles from spherical to ellipsoidal. Ellipsoidal particles demonstrated stronger long-range inter-particle capillary attractions between the solute particles, thereby leading to more uniform distribution, (4) introducing surface acoustic waves (SAWs) into evaporating droplets. This strategy is essential to trap solute particles on the substrate rather than moving forward to the edge by applying a pressure gradient at the surface, and (5) last but not least, employing Marangoni flow to create a surface tension gradient over the liquid-air interfaces of the solute particle droplet. The Marangoni flow aids in forming a concentrated solute center after evaporation when it is applied inward to the solute particle droplet to overcome outward capillary flow.

The formulation of printable ink with functional materials for sensing applications is an extremely important revelation for printed sensors. It allows for direct sensor printing without adding an extra step of sensor surface modification as shown in Figure 3b. Furthermore, with this innovative ink formulation, the functional moieties on top of the sensing electrode can also be more homogenous, and the printed sensor has a higher chance for reproducibility. In principle, printable ink for sensors mainly comprises active materials, binders, additives, and solvents. The main components of the ink are active materials including carbon black materials [69], semiconductor nanomaterials [70], conductive materials [71], electroactive materials [72] and so forth. The sensing material, such as biocompatible materials (enzyme, DNA, aptamer), polymers, various gels, and metals, is incorporated into the active electrode materials to function as sensing probes to detect the anticipated target and increase the electrocatalytic activity of the sensor electrode. Diversiform printable materials have greatly broadened the horizons of printed sensors as analytical and diagnostic tools for both research and commercial purposes. There have been a few attempts to tailor ink composition with functional materials for sensing purposes. For example, enzyme-containing inks are used for enzyme-based electrode sensor direct printing. The primary concern with enzyme ink is that it has a low shelf life on account of enzymes in suspension tending to rapidly lose their catalytic activity. Another potential disadvantages of printing electrodes using the enzyme-containing ink are the absorption of non-specific binding (NSB) and stability loss during the printing process as a consequence to thermal and mechanical stress [73]. To solve these problems, considerable work has been done to promote better stability and catalytic activity of the enzyme in the ink admixture, for instance, by employing an additive, using “immobilized enzyme”, enzyme rigidification, and fine-tuning enzyme attachment [74–76]. Direct sensor printing with customized ink containing polymers has also been reported. Bardpho et al. customized

homemade graphene-polyaniline (G-PANI) ink to modify screen-printed carbon electrodes (SPCEs) for chromatographic determination of antioxidants in teas [77]. The G-PANI layer was inkjet-printed on the working electrode of the SPCE. In this work, PANI material was used to not only increase the electron transfer kinetics of the sensor electrode when combined with graphene, but it also played a role in preventing graphene agglomeration and improving graphene distribution on the electrode surface. Teengam et al. used the same recipe as Bardpho et al. to prepare G-PANI ink for surface modifier of his electrochemical paper-based peptide nucleic acid biosensor for human papillomavirus [78]. This study employed three printing techniques: (1) wax printing to create a hydrophobic barrier on a paper substrate, (2) screen-printing to fabricate the three electrodes of the sensor system (WE, RE, and CE), and (3) inkjet printing to modify the working electrode with G-PANI. In another study, Kit-Anan et al. and colleagues synthesized PANI ink in the laboratory and used the ink to print over the carbon working electrode (WE) as a sensor modifier to determine ascorbic acid [79]. The modifier ink was solely PANI material, and it was printed using an ink-jet printer to achieve a homogenous PANI layer on the sensing surface (WE).

Electrodeposition of functional materials on sensor electrodes has been studied extensively in the past decades. To date, various methods of electrodeposition have been developed to integrate engineered nanomaterials directly onto sensor electrodes, including electrochemical, electrospinning, and electrospray. In this review, we would like to focus on electrochemical deposition as it is a cost-effective technique and a common method found in the literature to modify the sensing electrode of printed sensor compared to the other two electrodeposition methods. Nevertheless, the electrospinning and electrospray deposition techniques have been discussed in detail elsewhere [80,81]. Electrochemical deposition offers rapid synthesis time with the absence of oxidant and reductant [82]. Moreover, the modifier material is directly deposited on top of the working electrode (sensing area), and it provides better adhesion [83]. Electrochemical deposition is a facile deposition technique that can be done mostly at room temperature and does not require a high vacuum setup. Three electrodes (WE, RE, and CE) are dipped into a desired material solution, and sufficient excitation potential is applied to give an external force for ions in the solution to move and reduced at the working electrode. A schematic of an electrochemical deposition setup is shown in Figure 3c. Cyclic voltammetry, double-pulse deposition, and potential step are the frequently used techniques for electrochemical deposition reported in the literature [84]. In previous studies, Rodríguez-Sánchez et al. established that the deposition particle size can be controlled precisely by adjusting the current density or applied potential and electrolysis time [85]. Tu et al. fabricated a disposal biosensor using one-step electrochemically deposited reduced graphene oxide (OerGO) onto a SPCE [86]. This sensor was exploited for L-lactate detection, an early cancer biomarker. The authors reported a successful rapid detection of L-lactate using this OerGO/SPCE sensor with only a tiny amount of sample (10  $\mu$ L) within 10 s. Hondred et al. designed a printed graphene sensor for the direct and rapid monitoring of triple-O linked phosphonate organophosphates (OPs) [87]. The graphene electrode was printed using Inkjet Maskless Lithography (IML) technique, followed by electrodeposition of platinum nanoparticles (PtNPs dia.  $\sim$ 25 nm) to improve its electrical conductivity before conjugation with phosphotriesterase (PTE) enzyme for probing purposes. It has been observed that the sensitivity of the sensor improves as the number of deposition pulses or cycles increases (0 to 75 cycles, corresponding to sensor sensitivity of 195 and 275 nA/ $\mu$ M, respectively). Another study demonstrated the electrodeposition of flower-like gold microstructures (FLGMs) on top of the SPCE working electrode in sensor fabrication for serpin A12 detection [88]. To achieve superior sensor performance, the FLGM's deposition time was optimized to 150 s. Subsequently, serpin A12-specific thiolated aptamer was covalently on the FLGMs as a probe to detect serpin A12. The sensor exhibited good reproducibility, selectivity, and sensitivity, as well as stability.

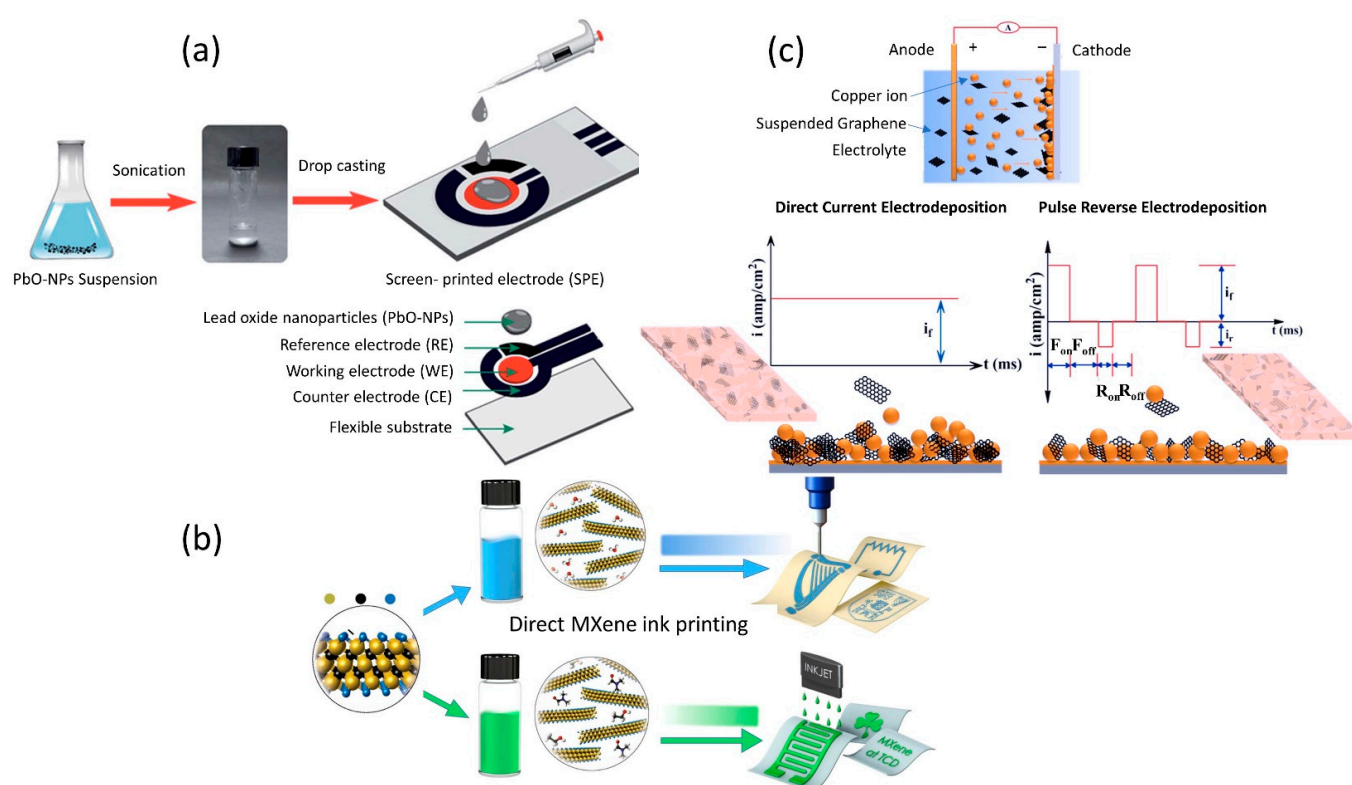


**Figure 3.** Surface modification or functionalization techniques of printed electrochemical sensors with nanomaterials. (a) Drop-casting technique. Reproduced/Adapted from Ref. [89] with permission from The Royal Society of Chemistry. (b) Ink-mixing and printing technique. Reprinted with permission from [90]. Copyright 2014 Springer Nature. Authors licensed under a Creative Commons Attribution (CC BY) license. (c) Electrodeposition technique. Reprinted with permission from [91]. Copyright 2019 Springer Nature. Authors licensed under a Creative Commons Attribution (CC BY) license.

#### 4. Transition Metal Dichalcogenides (TMDCs)

In recent years, there has been a greater focus placed upon transitional metal dichalcogenides (TMDC) within the sensor literature owing to their unique properties for sensing applications, such as excellent stability, biocompatibility, adjustable performance, fast heterogeneous electron transfer, and high specific surface area [92–94]. Moreover, TMDC materials also have the advantages of photothermal properties, fluorescent properties, and high density of electronic states making them popular for bioimaging [95–97].

The structure of TMDC materials is determined by one transition metal atom that is covalently linked with two hexagonal planes of chalcogen atoms in a sandwich fashion, which gives the material formulation of X-M-X, where M refers to transition metal atoms such as tungsten (W), molybdenum (Mo), titanium (Ti), and a few other metal atoms, while X represents chalcogen atoms such as sulfur (S), selenium (Se), and tellurium (Te). In the periodic table, Figure 4a,b exhibit the general structure of a single layer of TMDC material and TMDC elements (metal transition and chalcogen atoms), respectively. TMDC bulk consists of numerous layers of X-M-X stacked on top of each other and held together through Van der Waals force; therefore, the bonds between the adjacent layers are remarkably weak, although the chemical bond between atoms within each layer is strong and stable [98]. Interestingly, TMDC also possesses a wide range of electrical properties from insulator to superconductor, making it a promising material for an extensive range of applications. For example, HfS<sub>2</sub> is an insulator, MoS<sub>2</sub> is a semiconductor, WTe<sub>2</sub> and TeS<sub>2</sub> are semi metals, while NbS<sub>2</sub> and VS<sub>2</sub> belong to the true metals group [99].

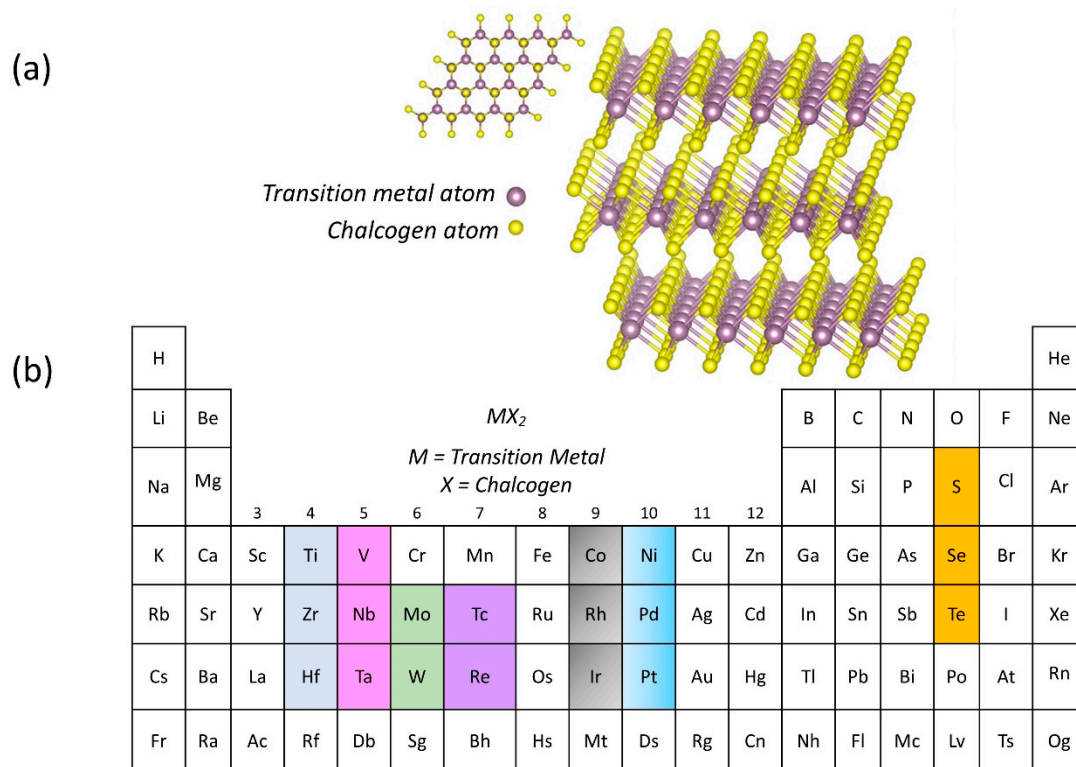


**Figure 4.** (a) General structure of TMDC, where the metal atom (purple) is sandwiched between two chalcogenides atoms (yellow). Reprinted with permission from [100]. Copyright 2021 Springer Nature. Authors licensed under a Creative Commons Attribution (CC BY) license. (b) There are more than 40 combinations of transition metal and chalcogen atoms that can form stable TMDC materials. The transition metals and the three chalcogens elements are highlighted in the periodic table.

#### 4.1. Molybdenum Disulfide ( $MoS_2$ )

Among all the TMDC materials, molybdenum disulfide ( $MoS_2$ ) is the most popular material for sensing applications in the TMDC family, owing to its robustness. On top of that, high surface area and direct tunable bandgap makes  $MoS_2$  a promising candidate to extend the detection range with considerable responsivity [101]. In recent years, the direct printing method using nanomaterial inks to fabricate printable sensors has drawn more attention as this method offers time efficiency and is more suitable for sensor mass production. However, this method requires optimization at the ink development level, for example, at the viscosity recovery rate, flow behavior, and oscillatory modulus, to ensure the developed ink is adequate for the intended printer or printing process. Pavličková et al. [102] and her research group successfully fabricated a screen-printed  $MoS_2$  electrochemical sensor for dopamine sensing for the first time. Interestingly, the research group developed their own  $MoS_2$  ink before printing on the fluorine-doped tin oxide (FTO) substrate as sensor electrodes. In this work, they developed the ink with varying  $MoS_2$  particle size and volume to investigate the effect of these two parameters on dopamine sensing. The 6  $\mu m$  and 90 nm  $MoS_2$  particle sizes were examined in this study. The volume of 6  $\mu m$  particle size was 25, 45, and 60 (measured in wt% units), and for 90 nm particles, it was 25 and 45 wt%, as the volumes higher than 45 wt% were not miscible in nanopowder form. The sensing properties of their  $MoS_2$  electrodes were evaluated in a 0.1 M phosphate buffer solution (pH 7.0) with the presence of dopamine. The DPV curve was used to determine the electrochemical oxidation of dopamine and the linear dependence of oxidation peak current vs. dopamine concentration in the range up to 300  $\mu M$ . The authors reported the performance of 6  $\mu m$  particles of  $MoS_2$  and a volume of 45 wt% (Mo6-45) gave the best performance in response to dopamine presence with LOD value of 246 nM and sensitivity

of  $5.00 \times 10^{-8}$  A  $\mu\text{M}$ . The other modified MoS<sub>2</sub> electrodes' performance is summarized in Table 1.

**Table 1.** Performance of MoS<sub>2</sub> ink towards dopamine sensing in the work of Pavličková et al. [102].

MoS <sub>2</sub> Ink Sample	MoS <sub>2</sub> Particle Size	Volume (wt%)	LOD	R <sup>2</sup>
Mo6-45	6 $\mu\text{M}$	45	246 nM	0.996
Mo6-25	6 $\mu\text{M}$	25	686 nM	0.995
Mo6-60	6 $\mu\text{M}$	60	669 nM	0.975
Mo90-25	90 nM	25	456 nM	0.982
Mo90-45	90 nM	45	865 nM	0.976

Owing to its large surface area, 2D MoS<sub>2</sub> material is frequently used on the WE of electrochemical sensor for direct detection. Asefifeyzabady et al. [103] carried out a study of MoS<sub>2</sub>-based electrochemical sensor for detection of trinucleotides CGG repeats, which are crucial for combating a variety genetic disorders. It is a three-electrode system, where the counter and pseudo electrodes were inkjet-printed with silver nanoparticles (AgNPs), and the WE was drop-casted with their laboratory prepared MoS<sub>2</sub> solution on top of the AgNPs electrode. The detection of the CGG on the MoS<sub>2</sub> WE surface relied on the current response in the presence of  $[\text{Fe}(\text{CN})_6]^{-3/-4}$  using DPV analysis method. In their paper, Asefifeyzabady et al. discovered two important aspects of the DNA detection on the MoS<sub>2</sub> sensor surface. First, this study identified that the direct adsorption of DNA on the MoS<sub>2</sub> enhanced the electrocatalytic current with the number of CGG repeats length. This finding is pivotal and can be used to distinguish between normal and abnormal repeats length. Second, they found that the DNA duplex conformation would remain on the MoS<sub>2</sub> surface after hybridization and give rise the electrocatalytic current, resulting in an increase in the DPV oxidation. In contrast to previously published studies, Chu et al. [104] and Loo et al. [105] demonstrated a decrease in the oxidation peak current value of the DPV signal because the double-stranded DNA (dsDNA) formed by hybridization of probe DNA (pDNA) and complementary DNA (cDNA) had been released from the MoS<sub>2</sub> electrode surface. The proposed MoS<sub>2</sub>/SPE sensor exhibited successful detection of double-stranded CGG-8 (dsCGG-8) repeats using DPV analysis in the concentration range of 1 aM–100 nM and showed a good linear calibration curve ( $R^2 = 0.992$ ) with 3.0 aM LOD. Zribi et al. [106] described a voltammetry technique for measurement of tyrosine by employing SPCE and screen-printed gold electrodes (SPAuE) modified with MoS<sub>2</sub> nanomaterial. In it, 0.45  $\mu\text{g}/\text{mL}$  of MoS<sub>2</sub> dispersion was directly drop-cast on top of both SPE working electrodes as a modifier. The CV analyses on both SPCE and SPAuE showed that the tyrosine oxidation current peak intensity was enhanced proportionally to its concentration. On both modified SPEs with MoS<sub>2</sub>, the current signal was observed to enhance owing to the intrinsic electrocatalytic activity of 2D-MoS<sub>2</sub> [107]. The sensitivity of the SPCE and SPAuE sensors was  $1400 \mu\text{A} \cdot \text{mM}^{-1} \cdot \text{cm}^{-2}$  and  $1580 \mu\text{A} \cdot \text{mM}^{-1} \cdot \text{cm}^{-2}$ , respectively, in the linear range of 0–100  $\mu\text{M}$ . The LOD of the SPCE sensor was determined to be 31.23  $\mu\text{M}$ , while LOD of the SPAuE sensor was 0.5  $\mu\text{M}$ . Furthermore, the authors also carried out a chronoamperometric analysis to determine tyrosine with MoS<sub>2</sub>-modified SPCE under a constant voltage (0.6 V vs. Ag/AgCl). They reported that the oxidation current rapidly risen-up with tyrosine concentrations up to 617  $\mu\text{M}$ . The current-concentration curve exhibited dynamic linearity in the very low concentration range (0–50  $\mu\text{M}$ ), provided sensitivity of  $148 \mu\text{A} \cdot \text{mM}^{-1} \cdot \text{cm}^{-2}$  with LOD of 1.4  $\mu\text{M}$ . However, the present study has suffered from inadequate data. The authors only examined the detection of tyrosine on MoS<sub>2</sub>-SPCE sensor, there are no amperometric data reported for tyrosine detection on MoS<sub>2</sub>-SPAuE sensor device. Further research could usefully explore the performance of MoS<sub>2</sub>-SPAuE sensor in tyrosine detection using chronoamperometry analysis. The group reported further development of MoS<sub>2</sub>-SPCE sensor for simultaneous detection of dopamine (DA) and tyrosine (Tyr) in the presence of uric acid [108]. Similar to previous

work, Zribi et al. modified SPCE with MoS<sub>2</sub> via direct drop-casting method on the WE. The detection of DA and Tyr was done in a buffer using cyclic voltammetry (CV) and linear sweep voltammetry (LSV) analysis. Data from CV analysis shows separation oxidation peak current of DA and Tyr at 0.16 V and 0.57 V, respectively. They also investigated current-concentration dependence of the SPCE on both the DA and Tyr target samples using LSV analysis technique. Both detections demonstrated linear fit in the range of 0–100 μM for DA and 0–500 μM for Tyr. The limit of detection for DA and Tyr was 0.085 μM and 0.5 μM, respectively. Further, the investigation of simultaneous detection of DA and Tyr has been carried out in the presence of uric acid (UA) using LSV technique. Their findings show three distinct peaks at different voltages. Additionally, they also reported LSV data with variations of UA, DA, and Tyr concentrations to examine the dependency of DA and Tyr detection in UA presence. Their result revealed that the detection of DA and Tyr was almost independent with or without the presence of UA. Tajik et al. synthesized MoS<sub>2</sub> nanosheets (MoS<sub>2</sub>-NSs) using a single-pot hydrothermal protocol and dispersed them on SPE to fabricate a MoS<sub>2</sub>-NSs sensor to detect isoniazid (INZ) and acetaminophen (AC). INZ is a commercially available medication that is routinely given as a treatment for tuberculosis (TB) patients. Long-term exposure to INZ may induce hepatotoxicity in people suffering from inflammation and may even cause fatality [109,110]. An overdose of AC (4 g/day) can lead to hepatotoxicity, nephrotoxicity, gastrointestinal problems, and tissue failure [111]. The main motivation of Tajik's work was based on the growing concern of liver damage because of INZ co-administered with AC. The prepared MoS<sub>2</sub>/SPE possessed excellent electrochemical properties with high current response and large active surface area of 0.16 cm<sup>2</sup> which was 5.1 times larger than the bare SPE. Figure 5a shows the FESEM image of the synthesized MoS<sub>2</sub> nanosheets. Accompanied by high catalytic activities and large active sites, the MoS<sub>2</sub>/SPE sensor demonstrated LOD of 10 nM and exhibited linear elevation with a wide range of INZ concentration (0.035–390 μM). In this work, Tajik also demonstrated simultaneous detection of INZ and in the presence of AC. Two separated and well-defined oxidation peaks were observed using DPV method, as shown in Figure 5b, suggesting that the MoS<sub>2</sub>/SPE sensor potentially allowed for simultaneous detection. It can be seen that the sensor has good stability, as the peak current of INZ remained stable even after 4 weeks. Furthermore, the sensor showed a good mean relative standard deviation (RSD) value, capable of real sample analysis. In a separate study, Neethipathi et al. proposed a MoS<sub>2</sub>/SPE for heavy metal ions copper (Cu<sup>2+</sup>) detection [112]. The electrochemical electrode was printed using carbon paste by Screen Stencil Printer C920 (AUREL Automation) on flexible polyvinyl chloride (PVC) substrate. Sensing area modification was done by drop-casting solution of MoS<sub>2</sub> in dimethylformamide (DMF) on the working electrode. Using DPV analysis, the sensor successfully recognized the Cu<sup>2+</sup> in the linear concentration range of 5 μM to 1000 μM with LOD of 0.3125 μM. Additionally, the sensor showed excellent stability and repeatability by exhibiting a very small current deviation (less than 0.5%) during the course of 40 continuous cycles of CV analysis in PBS solution containing 100 μM of Cu<sup>2+</sup>. Due to its robustness, this sensor provides an optimistic future route for the electrochemical sensor development for heavy metal ions in harsh industrial waste. Compared to the recently published article on single- and multi-walled carbon nanotubes (SWCNTs and MWCNTs) modified SPE for the detection of quinone-based industrial pollutants, the proposed sensor by Neethipathi et al. was inferior in terms of sensitivity. The SWCNTs and MWCNTs modified SPE had lower LOD values of 0.04 μM and 0.07 μM, respectively [113]. However, it must be noted that the comparison is established only on the sensitivity of the sensing materials for industrial pollutant detection in general. Further exploration of MoS<sub>2</sub> potential for the detection of quinone-based industrial pollutants is essential for a more fair comparison.

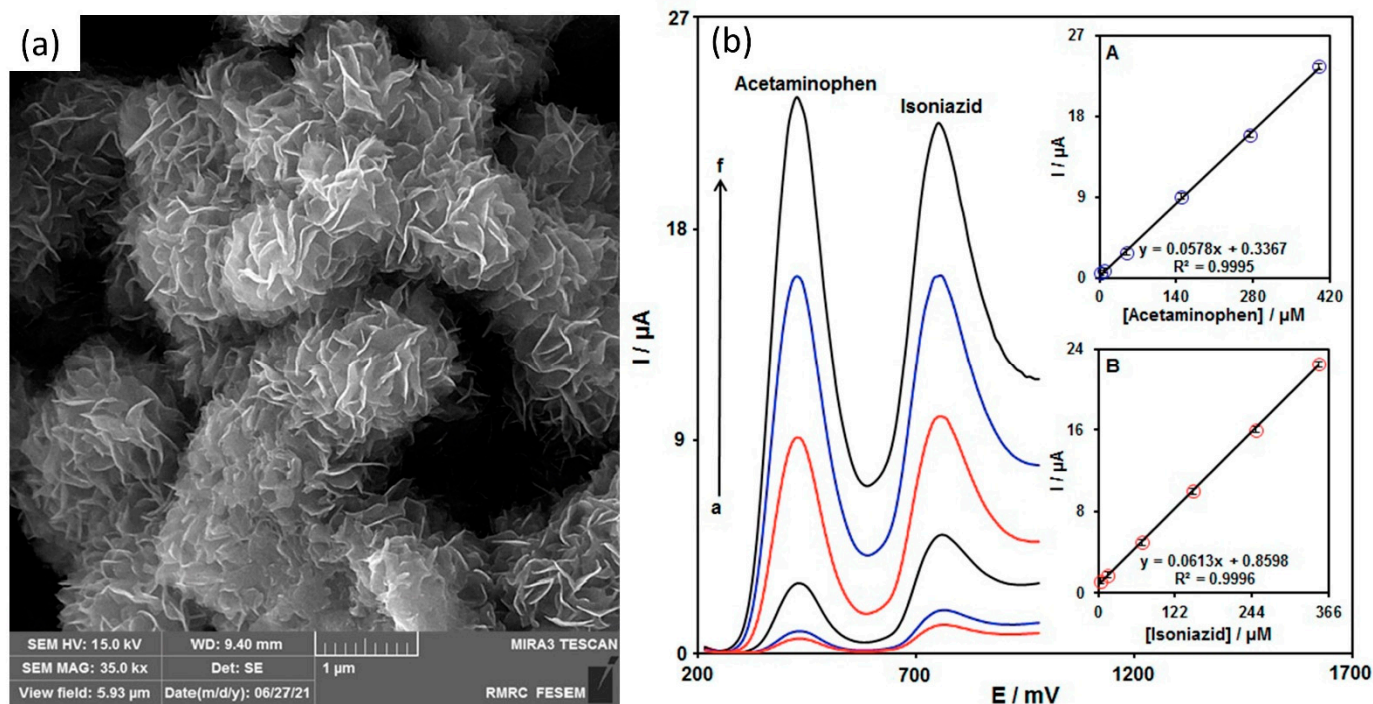


**Figure 5.** (a) FESEM image of MoS<sub>2</sub> nanosheets synthesized in Tajik et al.'s laboratory. (b) Differential pulse voltammetry of simultaneous detection of INZ and AC on MoS<sub>2</sub>-NSs/SPE. Inset (A): The anodic peak current plot vs. AC concentration. Inset (B): The anodic peak current plot vs. INZ concentration. Reprinted with permission from [114]. Copyright 2022 MDPI. Authors licensed under a Creative Commons Attribution (CC BY) license.

Efficient MoS<sub>2</sub> nanocomposites combined with SPE designed for low-cost manufacture could lead to a potentially commercially viable, reproducible, and sensitive sensor device. This has been demonstrated in recent years by Demir et al. [115], who used SPE based on MoS<sub>2</sub>-TiO<sub>2</sub>/rGO nanocomposites to determine AC in paracetamol using DPV for signal interpretation. Following the common technique that has been used by many researchers, Demir et al. prepared the SPE for AC detection by drop-casting dispersion of MoS<sub>2</sub>-TiO<sub>2</sub>/rGO on the working electrode. They reported that the DPV signal (current peak) of MoS<sub>2</sub>-TiO<sub>2</sub>/rGO/SPE was linearly proportional to the concentration of AC in the range of 0.1 μM to 125 μM. The LOD of the sensor was 0.046 μM. Moreover, their sensor also surpassed the sensitivity of most other sensors that have been reported in the literature for detection of AC with sensitivity value of 0.4425 μA μM<sup>-1</sup>. The excellent sensing performance demonstrated by this sensor was attributed to MoS<sub>2</sub>-TiO<sub>2</sub>/rGO nanostructure. The MoS<sub>2</sub> sandwich structures have provided unsaturated edge sites for surface functionalization [116], and the regulation band structures, consequently boosted the sensor performance [117], while TiO<sub>2</sub> has been utilized in the composition to enhance the electrocatalytic effect on the electrode surface [118], coupled with rGO, which served for efficient electron transfer and high surface area for sensing purposes [119]. Beyond that, there are another few likely reasons that contributed to such excellent sensing performance: (1) interfacial properties of MoS<sub>2</sub> nanoparticles with rGO sheets in the structure of composite create a synergetic effect, (2) high electrical conductivity of rGO nanosheets, and (3) enhancement in the surface area leading to an increment in the electrocatalytic activity of MoS<sub>2</sub>-TiO<sub>2</sub>/rGO owing to inhibition of nanomaterial aggregation. Their sensor exhibited excellent selectivity and sensitivity as well as recovery for direct diagnosis of AC in drug and real human urine samples. Gui et al. developed chemically exfoliated MoS<sub>2</sub>(ce-MoS<sub>2</sub>)/silver nanorods (AgNRs)-modified SPE immunosensor for prostate-specific antigen (PSA) detection [120]. In this study, negatively charged ce-MoS<sub>2</sub> and positively charged AgNRs dispersion were integrated onto the SPE working electrode to form a nanostructured

surface, in which the anti-PSA antibodies were directly immobilized. It is worth mentioning that the AgNRs were anchored onto the MoS<sub>2</sub> nanosheets' surface via cetyltrimethylammonium bromide (CTAB), which altered the AgNRs' electrical properties and, accordingly, expedited amalgamation of AgNRs on MoS<sub>2</sub> nanosheets via electrostatic interaction. The electrochemical impedance spectroscopy (EIS) data analysis exhibited a wide detection range of 0.1 to 1000 ng mL<sup>-1</sup> with high reproducibility and good stability for 21 days at 4 °C. The detection limit of this MoS<sub>2</sub>/AgNRs sensor was 0.051 ng/mL. Another interesting SPE biosensor using MoS<sub>2</sub>-based nanocomposite was reported by Sadeghi et al. [121]. This biosensor was designed with PANI/MoS<sub>2</sub> nanocomposites as sensing materials for molecular identification of Guanine (G), Adenine (A), Thymine (T), and Cytosine (C) nucleobases (DNA nucleobases). The research group performed a simultaneous detection of G, A, T, and C nucleobases in quaternary solutions and reported the DPV oxidation peak currents of all the DNA nucleobases were approximately linear. The detection of G and A were linear in the range of 0.1–10 μM, while the detection of T and C also demonstrated good linear results, but in a different range (1.2–100 μM). However, the linear regression of calibration curves showed inconsistency when the G, A, T, and C nucleobases were quantified individually. According to the authors, these findings may reflect the change in control factor of the sensing electrode surface. As for G and A nucleobases, the surface reaction at low concentration was controlled by diffusion processes, while at high concentration, the surface reaction was governed by the absorption process. In contrast to C nucleobase, an inverse finding was observed. The research, however, is limited by the lack of information and clarity on the individual determination of T nucleobase. The LOD of G and A was 0.015 mol L<sup>-1</sup> when quantified individually as well as in a quaternary solution, while the LOD of T and C was reported to be 0.14 mol L<sup>-1</sup> when quantified in both conditions. This PANI/MoS<sub>2</sub>-nanocomposite-based biosensor revealed noteworthy electrocatalytic activity for G and A nucleobase oxidation as it demonstrated the highest peak oxidation current compared to bare CPE, MoS<sub>2</sub>/CPE and PANI/CPE. This could be attributed to the strong  $\pi$ - $\pi^*$  interaction and electrostatic adsorption, leading to an efficient electron change between the free bases and the electrode surface. The biosensor confirmed its stability and reproducibility with RSD for quantification of A and G of 4.06% and 3.76%, respectively. In another study, graphene was mixed with MoS<sub>2</sub> and dispersed together to create a nanocomposite for determination of trans-resveratrol (TRA) in red wine using SPE sensor [122]. In this approach, MoS<sub>2</sub> layer was synthesized on the surface of graphene layers to form sheet-on-sheet graphene-MoS<sub>2</sub> (Gr-MoS<sub>2</sub>) nanocomposite, which was later deposited on top of the SPE working electrode. Here, the Gr-MoS<sub>2</sub> acts as a matrix for direct sensing of TRA from a wine sample. It should be noted, however, that the TRA sample required pre-treatment, such as extraction from wine, before being electrochemically quantified using this sensor. Using square wave voltammetry (SWV) technique, the sensor successfully recognized the TRA concentration from 1.0 to 200 μmol L<sup>-1</sup> with 0.45 μmol L<sup>-1</sup> LOD.

Turning now to the experimental evidence on decorated MoS<sub>2</sub> as a sensing material. Generally, MoS<sub>2</sub> exists as two kinds of crystalline phases: 2H phase (2H-MoS<sub>2</sub>) and 1T phase (1T-MoS<sub>2</sub>). The 1T-MoS<sub>2</sub> has been reported to exhibit higher conductivity and superior charge transfer ability, attributed to its metallic property [123]. Moreover, it also possesses higher catalytic activity because both the edges and basal plane are catalytically active [124]. For this reason, modification of electrochemical sensor with 1T-MoS<sub>2</sub> has demonstrated excellent sensing performance, surpassing that of electrochemical sensor modified with 2H-MoS<sub>2</sub> [125]. Despite its advantages for electrochemical applications, 1T-MoS<sub>2</sub> is a metastable material, and its mechanisms for stable performance are yet to be clarified [126]. In contrast to 1T-MoS<sub>2</sub>, 2H-MoS<sub>2</sub> has more stability with semiconductive property [127]. However, it suffers from low density of active sites and poor electrical transport property. Experimental evidence has established that the catalytically active sites of 2H-MoS<sub>2</sub> monolayer are generally located only at the edges and corners, whereas its basal atoms are catalytically inert [128], consequently limiting the catalytic performance of the 2H-MoS<sub>2</sub>. Er

et al. carried out a study on 1T-MoS<sub>2</sub> decorated with shape-dependent gold nanostructures for determination of doxorubicin (DOX) [129]. In this work, a SPE surface was modified with single-crystal gold nanospheres (AuNSPs) and nanorods (AuNRDs). These golds were decorated separately on 1T-MoS<sub>2</sub> layer on top of the SPE WE and their electrocatalytic activity towards DOX was analyzed. Taking an evidence-based approach, Er et al. showed that the 1T-MoS<sub>2</sub>/AuNRDs exhibited better electrocatalytic efficiency as a sensing material compared to 1T-MoS<sub>2</sub>/AuNSPs. Their CV analysis revealed that the SPE with 1T-MoS<sub>2</sub>/AuNRDs had the narrowest peak-to-peak separation ( $\Delta E_p$ ) and larger anodic and cathodic for Fe(CN)<sub>6</sub><sup>3-/4-</sup> compared to bare SPE and 1T-MoS<sub>2</sub>/AuNSPs/SPE, implying that the 1T-MoS<sub>2</sub>/AuNRDs has the fastest electron transfer capability between probe molecules and the SPE surface. It is noteworthy that the redox peaks that have been observed corresponded to the oxidation of hydroquinone and the reduction of quinone groups that occupied the center of DOX structures [130]. Furthermore, the 1T-MoS<sub>2</sub>/AuNRDs/SPE sensor exhibited high sensitivity of 7.13  $\mu\text{A } \mu\text{M}^{-1} \text{cm}^{-2}$  towards the DOX assay and excellent LOD (2.5 nM) with a linear range between 0.01 to 9.5  $\mu\text{M}$ . The sensor has also shown remarkable selectivity in real samples analysis. This sensor was successfully used for direct detection of DOX in human blood serum without pre-treatment. In another study, 2H-MoS<sub>2</sub> nanosheets (MoS<sub>2</sub> NSs) decorated with controlled density of mono dispersed small gold particles (AuNPs@MoS<sub>2</sub>) for detection of miRNA was reported [131]. Here, the sensing strategy that was used in this approach was upon hybridization of capture probe ssDNA (CP) with target miRNA sequence (TR), alongside with complementary ssDNA sequence (AP) that served as signal amplification. These elements were mainly immobilized into the AuNPs@MoS<sub>2</sub> screen-printed gold electrode (SPGE) transducer by absorption. The quantification of miRNA was done by chronocoulometry (CC) technique based on the number of cationic redox molecules [Ru(NH<sub>3</sub>)<sub>6</sub>]<sup>3+</sup> that were electrostatically associated with the anionic DNA backbones. In a study conducted by Steel et al. [132], it was shown that one [Ru(NH<sub>3</sub>)<sub>6</sub>]<sup>3+</sup> cationic redox marker was electrostatically trapped for every three nucleotide phosphate groups. This study also assesses the significant differences in thickness and size of MoS<sub>2</sub> platelets. They discovered that the AuNP@MoS<sub>2</sub>/SPGE sensor with the thinnest and smallest MoS<sub>2</sub> nanosheets has superior performance compared to larger and thicker MoS<sub>2</sub> nanosheets. The LOD of AuNP@MoS<sub>2</sub>/SPGE sensor with the thinnest and smallest MoS<sub>2</sub> nanosheets was down to 100 aM, which is 2 orders of magnitude lower than bare gold (Au) electrode. In addition to that, the sensor also demonstrated a 25% enhancement in DNA-miRNA hybridization efficiency. Singhal et al. and co-workers carried out a series of experiments to investigate potential of MoS<sub>2</sub> on screen-printed gold electrode sensor (MoS<sub>2</sub>/SPGE) to detect chikungunya virus [133]. This prototype used hybridization of DNA on the MoS<sub>2</sub>/SPGE as a determinant for sensor detection. The fabrication of the DNA-based sensor for chikungunya virus detection on MoS<sub>2</sub>/SPGE was demonstrated as in Figure 6a. Probe DNA was simply immobilized on the SPGE sensing areas that were coated with MoS<sub>2</sub>, followed by target DNA and methylene blue (MB). The addition of MB in this experiment step allowed for electrochemical response enhancement. The biosensor response was recorded using voltammetry technique, where they observed that the potential was shifted to the negative side with immobilization of the probe DNA and reverted to the positive side upon hybridization with the target DNA, as shown in Figure 6b. This finding is likely to be related to the negatively charged nature of DNA and electron transfer during the hybridization process [134]. This phenomenon can be explained as follows. The MoS<sub>2</sub> surface and MB undergo a redox reaction during cyclic voltammetry to produce the characteristic voltammogram at a specific potential. Immobilization of probe DNA on MoS<sub>2</sub> surface altered the electron transfer, resulting in decreased potential and making the MB easier to reduce (potential shifted to the negative side). When the target DNA was added onto the MoS<sub>2</sub> surface, hybridization occurred, causing restructuring molecules, and called for more electrons to reduce the MB. However, fewer electrons were available for reducing MB, resulting in an increased reduction potential (potential reverting to the positive side). The biosensor's performance was validated by quantifying the target

oligonucleotides in a serum sample and was shown to be a successful detection via EIS technique (Figure 6c). The LOD of this biosensor was 3.4 nM with a linear range of 0.1 nM to 100  $\mu$ M.

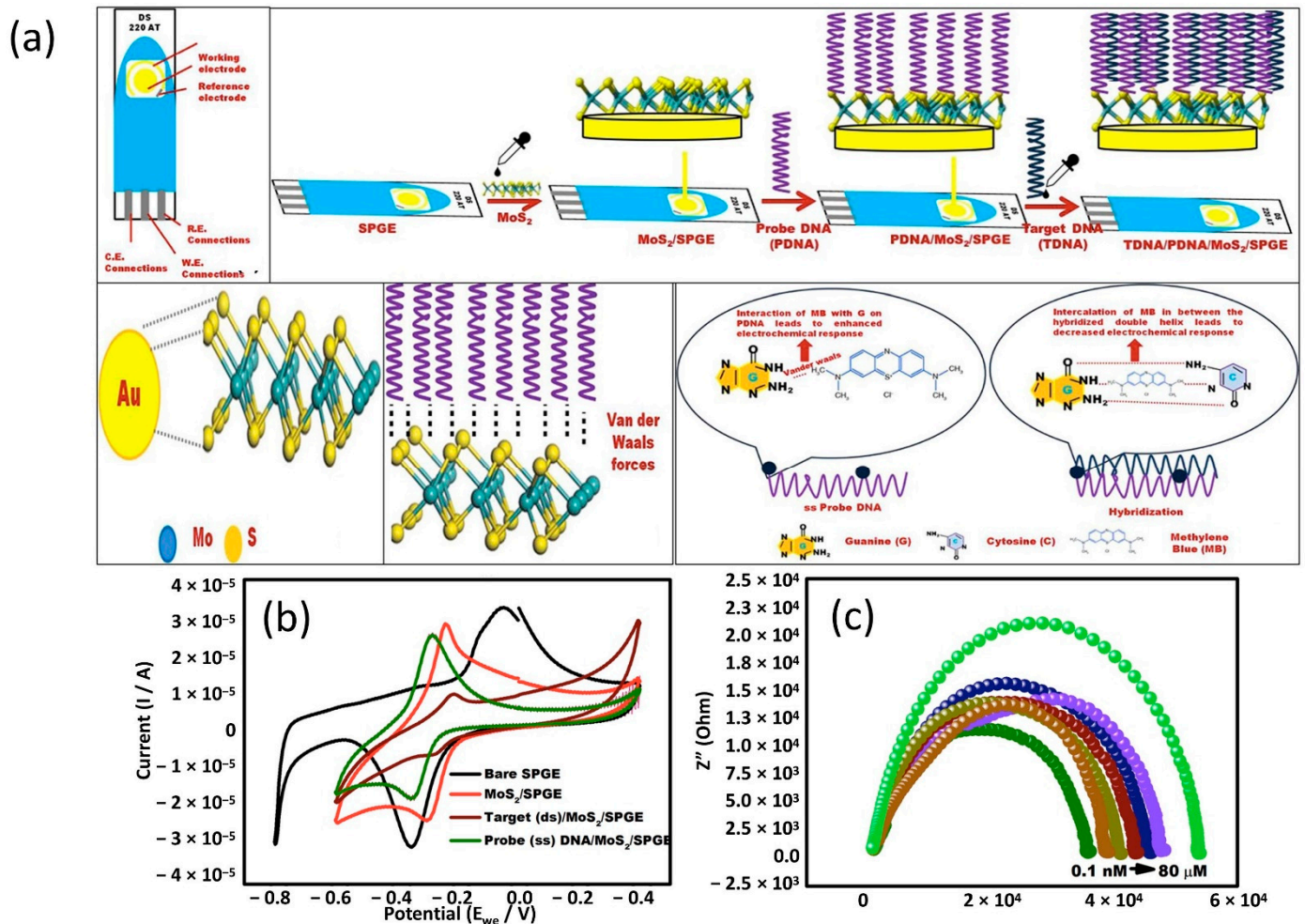


**Figure 6.** (a) From left to right, fabrication steps of MoS<sub>2</sub>/SPGE sensor for chikungunya virus. Step-wise shows fabrication of SPGE with MoS<sub>2</sub> nanosheets, immobilization of probe DNA and target DNA. The next illustration shows strong affinity interaction of Au and S (in MoS<sub>2</sub>), Van der Waals interaction between probe DNA and the MoS<sub>2</sub> surface, principle for the detection of target DNA via redox hybridization indicator, i.e., methylene blue. (b) Comparison of cyclic voltammogram graph of bare SPE, MoS<sub>2</sub>/SPE, Target/MoS<sub>2</sub>/SPE, and Probe/MoS<sub>2</sub>/SPE. (c) Nyquist Plot verifying hybridization of the different concentration of the complementary target DNA at PDNA/MoS<sub>2</sub>NSs/SPGE. Reprinted with permission from [133]. Copyright 2018 Springer Nature. Authors licensed under a Creative Commons Attribution (CC BY) license.

As a different approach, MoS<sub>2</sub> also has been utilized as biomarker labels for signal amplification, to improve sensitivity of an immunosensor. Arévalo et al. [135] have integrated this concept into their amperometric multiplexed immunosensor for the determination of B cell activation factor (BAFF) and proliferation-induced signal (APRIL) immunity-related cytokines. In this work, screen-printed dual carbon electrodes (SPdECs) are modified with the biotinylated capture antibodies cAB<sub>BAFF</sub> and cAB<sub>APRIL</sub> on their respective working electrodes. This proposed sensor employs sandwich-type modes of operation, where a layer of antibody binds with analyte-antigen, which then binds with second labeled-antibody. A major advantage of this mode of operation is that it allows for measuring large antigens that are capable of binding two different antibodies. Both biomarkers BAFF and APRIL were

detectable in buffer at concentrations ranging from 0.24 to 120 ng mL<sup>-1</sup> ( $r^2 = 0.999$ ) and 0.19 to 25 ng mL<sup>-1</sup> ( $r^2 = 0.997$ ), respectively. The dual-immunosensor provided theoretical limit of detection of 0.08 for BAFF and 0.06 ng mL<sup>-1</sup> for APRIL. The sensor device has excellent selectivity and recognized both cytokines in cancer cell lysates and serum samples (diluted 10 times) from patients diagnosed with autoimmune diseases and cancer. In this investigation, Arévalo et al. employed MoS<sub>2</sub> as biomarker carrier tags instead of WE (sensing area) modifier. The role of MoS<sub>2</sub> in this work was specifically for carrier labels for signal amplification to improve the immunosensors' sensitivity. For a proper understanding of this sensor detection principle, a schematic of the fabrication sensor protocol is shown in Figure 7. Other works of MoS<sub>2</sub> on printable sensor are summarized in Table 2.

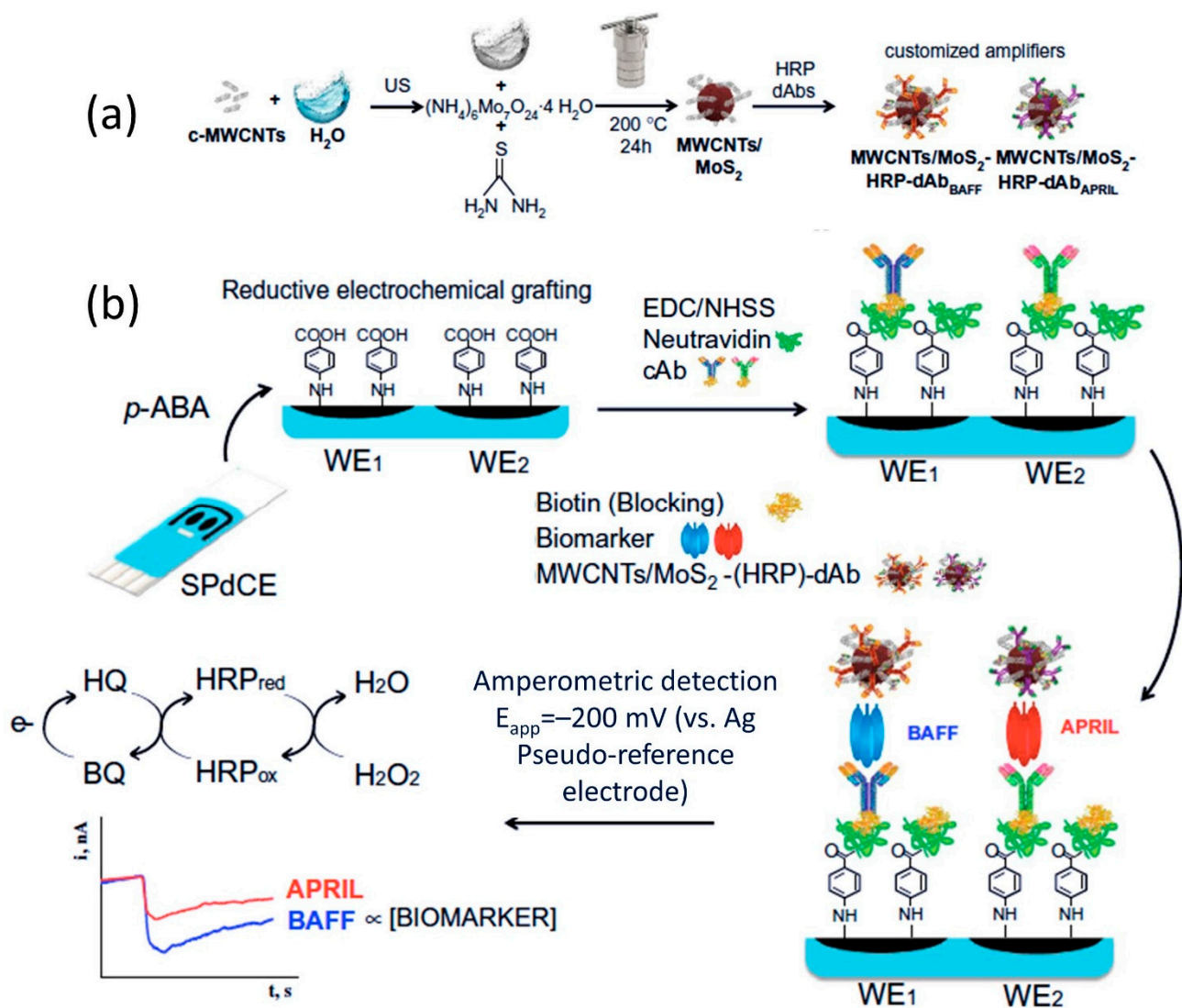


**Figure 7.** (a) A schematic of the fabrication of MWCNTs/MoS<sub>2</sub>-(HRP)-dAb nanocarriers and (b) their application on screen-printed dual carbon electrodes (SPdECs) for the determination of BAFF and APRIL biomarkers. Reprinted with permission from [135]. Copyright 2022 Springer Nature. Authors licensed under a Creative Commons Attribution (CC BY) license.

**Table 2.** MoS<sub>2</sub> material applications on printed electrochemical sensor.

Electrode Structure	Target	SPE Modification Technique	Analysis Method	Linear Range	Detection Limit	Ref.
HM-Al <sup>3+</sup> -(2D-MoS <sub>2</sub> )/SPGrEs	Hydrazine	Drop-casting	Double pulse chronoamperometry	0–0.400 mM	1.05 µM	[136]
PANI/MoS <sub>2</sub> /SPE	Anti-cyclic citrullinated peptide (aCCP) antibodies	Drop-casting (MoS <sub>2</sub> ) and electrochemically polymerization (PANI)	SWV	0.25 and 1500.0 IU/mL	0.16 IU/mL (PBS) and 0.22 IU/mL (10% Human Serum)	[137]
MoS <sub>2</sub> /PPyNPs/SPE	Ampicillin	Drop-casting	Amperometric	50–250 pg/L	10 pg/L (0.28 pM).	[138]
PMO-NiO/MoS <sub>2</sub> /SPCE	Cholesterol	Drop-casting and MO-polymerization	DPV	1 to 15 mg/dL	0.24 mg/dL	[139]
MoS <sub>2</sub> /CA/SPE	Troponin I	Electrospinning	EIS	10 fM to 1 nM	10 fM	[140]
RGO/MoS <sub>2</sub> /SPE	Cd <sup>2+</sup> , Hg <sup>2+</sup> , Pb <sup>2+</sup> in rice	Drop-casting	DPV	5 to 160 µM (Cd <sup>2+</sup> ) 5 to 160 µM (Hg <sup>2+</sup> ) 10 to 3000 µM (Pb <sup>2+</sup> )	49.83 µM (Cd <sup>2+</sup> ) 36.94 µM (Hg <sup>2+</sup> ) and 733.90 µM (Pb <sup>2+</sup> )	[141]
CA-MoS <sub>2</sub> /SPE	Acute Myocardial Infraction (AMI)	Drop-casting	EIS	10 fM to 1 nM	10 fM	[142]
AChE@CHIT/TiO <sub>2</sub> /MoS <sub>2</sub> /SPE	Monocrotophos pesticide	Electrodeposition and drop-casting	DPV	50 pM to 10 nM	50 pM	[143]
Probe-SH/MoS <sub>2</sub> /SPCE	Listeria or SARS-CoV-2	Drop-casting	DPV	NR	67.0 fM (Listeria) and 1.01 fM (SARS-CoV-2)	[144]
Co@MoS <sub>2</sub> /rGO/SPE	Glucose	Drop-casting	Amperometric	0 to 0.8 mM	30 nM	[145]
SPE-CB/MoS <sub>2</sub>	Cocoa catechins	Drop-casting	CV and DPV	0.12 to 0.25 µM	0.17 µM	[146]

NR: Not reported, MoS<sub>2</sub>: molybdenum disulfide, SPE: screen printed electrode, SPCE: screen printed carbon electrode, SPE-CB: carbon black SPE, SPGrEs: screen printed graphene electrodes, SWV: square-wave voltammetry, DPV: differential pulse voltammetry, EIS: electrochemical impedance spectroscopy, CV: cyclic voltammetry, HM-Al<sup>3+</sup>: hematin-aluminum complex, PANI: polyaniline, PPyNPs: PPyNPs: polypyrrole nanoparticles, PMO: poly (methyl orange), NiO: nickel oxide, CA: cellulose-acetate, AChE: acetylcholinesterase, CHIT: chitosan, TiO<sub>2</sub>: titanium oxide, Probe-SH: thiolated synthetic DNA sequence probe, Co: cobalt, rGO: reduced graphene oxide.

#### 4.2. Molybdenum Diselenide (MoSe<sub>2</sub>)

Similar to any other TMDCs material, molybdenum diselenide (MoSe<sub>2</sub>) exists in a sandwich structure, which comprises of one Mo covalently bonded with two chalcogen atoms of selenide (Se), and each monolayer is held by a weak force. Compared to its counterpart (MoS<sub>2</sub>), MoSe<sub>2</sub> has superior electrocatalytic reaction and specific conductance on account of twenty orders greater metallic conductivity, more functional unsaturated sites of selenides, attractive energy density, a faster electrochemical reaction rate, higher metallic binding with transition metals, and a larger atomic size [147–149]. With these fascinating properties, MoSe<sub>2</sub> has been widely used in various electrochemical applications [150–152].

A recent study reported the application of MoSe<sub>2</sub> on SPE as a disposable and portable sensor for detection of hydrogen peroxide (H<sub>2</sub>O<sub>2</sub>) in ultra-wide pH [153]. Other than the extraordinary properties listed above, MoSe<sub>2</sub> also has a small bandgap (~1.2 eV) and large interlayer spacing, which particularly favors the reduction of H<sub>2</sub>O<sub>2</sub> [154,155]. However, in spite of the great electrochemical properties, the MoSe<sub>2</sub> basal plane generally has poor conductivity and lack of active sites, which thereby hinders binding with -OH intermediate. To overcome this challenge, defect engineering and heteroatomic doping strategies were used to introduce strain and vacancies on the MoSe<sub>2</sub> basal plane. The MoSe<sub>2</sub> was synthesized by hydrothermal method, and further introduced to argon (Ar) and nitrogen

(N<sub>2</sub>) plasma treatments to create new active sites to enhance its catalytic performance. The defect MoSe<sub>2</sub> evidently has stronger -OH binding and on its surface when the SPE sensor has accomplished higher sensitivity and selectivity. For H<sub>2</sub>O<sub>2</sub> sensing, the SPE sensor was operated amperometrically at −0.30 V vs. saturated calomel electrode (SCE). The finding shows that the current response curve was linearly increased with H<sub>2</sub>O<sub>2</sub> concentration in the range of 0.02–0.2 mmol/L (at low concentration) and 0.2–20 mmol/L (at high concentration). This electrical signal response was generated from the reduction of H<sub>2</sub>O<sub>2</sub> to H<sub>2</sub>O. The sensitivity of the sensor was calculated to be 16.22 μA/(mM·cm<sup>2</sup>) and 15.68 μA/(mM·cm<sup>2</sup>) at low and high concentrations, respectively. This sensor achieved detection limit of 462.4 nmol/L. In separate work, Ramaraj et al. performed a series of experiments to show the doping effect of MoSe<sub>2</sub> in sensing applications, and further reported an iron (Fe)-doped MoSe<sub>2</sub>/SPE sensor for mesalamine (MES) determination, an anti-inflammatory agent in paramedical sample [156]. The MoSe<sub>2</sub> was doped with Fe using three different synthesis methods, which were hydrothermal, microwave-assisted synthesis, and chemical synthesis. Each of the Fe-doped MoSe<sub>2</sub> products were drop-casted onto separate SPEs to assess their electrochemical performance. SPE that is drop-casted with Fe-doped MoSe<sub>2</sub> via hydrothermal, microwave-assisted, and chemical synthesis is denoted as H-FeMoSe<sub>2</sub>/SPE, M-FeMoSe<sub>2</sub>/SPE, and C-FeMoSe<sub>2</sub>/SPE, respectively. From their findings, H-FeMoSe<sub>2</sub>/SPE has the highest electrocatalytic, superior sensing performance, and lowest detection limit compared to M-FeMoSe<sub>2</sub>/SPE and C-FeMoSe<sub>2</sub>/SPE. The relevance of these enhanced sensor performances was clearly supported by their EIS and CV data, where the H-FeMoSe<sub>2</sub> has the lowest R<sub>CT</sub> value, suggesting faster electron transfer and the highest current response, as well as the narrowest peak-to-peak separation in CV analysis, attributed to improved charge transfer conductivity. The determination of MES was analyzed by CV technique. The sensing mechanism relied on the conversion of MES to quinone-imine. As they concluded, H-FeMoSe<sub>2</sub>/SPE has the sharpest and highest oxidation peak current response in comparison to the other two FeMoSe<sub>2</sub>/SPE (M-FeMoSe<sub>2</sub>/SPE and C-FeMoSe<sub>2</sub>/SPE). This result may reflect differences in layer structure, thickness, and quality of the Fe-doped MoSe<sub>2</sub>. Moreover, the oxidation peak current was linearly increased with MES concentration in the ranging from 0.09 to 0.654 mM in N<sub>2</sub> purged buffer (pH 7). The selectivity of the sensor was also excellent as it yielded less than 5% current change with the presence of interferences. This H-FeMoSe<sub>2</sub>/SPE was tested for its ability to determine the presence of MES in Pentasa tablet. The analysis is done using DPV method, and they found out that the sensor was capable of quantifying MES in Pentasa solution, with 101.1–104% recovery and RSDs ranging from 2.1 to 2.7%.

#### 4.3. Tungsten Disulfide (WS<sub>2</sub>)

One of the most important constituents in any sensor device is a large surface area with very a good sensing matrix, and in recent years, the 2D material tungsten disulfide (WS<sub>2</sub>) has attracted considerable attention for this kind of application. WS<sub>2</sub> is a promising material candidate for future electronic and optoelectronic sensor applications owing to its unique combination of outstanding properties such as its 2D ultrathin atomic layer, high surface area, and good biocompatibility [157,158]. Furthermore, WS<sub>2</sub> also accommodates for self-assembly of thiolated compounds on its surface, which makes it more attractive compared to graphene material in terms of effortless surface modification [159]. WS<sub>2</sub> is one of the materials that belongs to the 2D TMDC group, in which the tungsten (W) layer is sandwiched between two sulfur layers (S) and stacked together by weak Van der Waals forces [160].

Mishra et al. developed an electrochemical paper-based analytical device (ePAD) based on WS<sub>2</sub>/aptamer hybrid, which provided a very selective approach for *Listeria monocytogenes* determination [161]. The ePAD was constructed on paper by screen-printed conductive carbon ink using silk mesh as a sensor pattern stencil. Different from any other printed sensor that has been reviewed in this article, Mishra's work presented an ePAD sensor with only two electrodes, WE and CE. The sensing matrix on this sensor prototype

was quite straight forward; WS<sub>2</sub> was drop-casted onto the WE and left to dry before aptamer immobilization. The incorporation of aptamer as a biological recognition element provides specificity for the impedimetric assay. Figure 8a exhibits the development of two electrode sensor on a paper substrate (ePAD), and Figure 8b demonstrates an ePAD sensor competitive assay for *Listeria monocytogenes* that was recorded with EIS technique. The EIS assessment data of this sensor revealed a correlation of *Listeria monocytogenes* concentration with the sensor's surface sensitivity, which provides a linear range of 10<sup>1</sup>–10<sup>8</sup> CFU/mL and a limit of detection of 10 CFU/mL. The use of WS<sub>2</sub> in combination with other functional materials as a sensing matrix offers the possibility of a new generation of highly specific, sensitive, selective, and reliable sensors for various detection. One practical work that combined not only one, but two functional materials with WS<sub>2</sub> as a sensing element was recently discussed by Pelle et al. [162]. The research group capitalized on the superior sensing layer of 2D WS<sub>2</sub> flakes decorated with catechin-gold capped nanoparticles (AuNPs-CT) and a carbon black-based screen-printed sensor for simultaneous determination of structural analogs of hydroxycinnamic acid (hCN); caffeic (CP), sinapic (SP), and *p*-coumaric acids (CM). The functional material, such as catechin-capped gold nanoparticles (AuNP-CT) was exploited to provide higher sensitivity and specificity, while the carbon black served as high conductivity and high electroactivity material. With regard to WS<sub>2</sub> flakes, they play a vital role in enhancing sensor performance by increasing the sensing surface area and electron transfer. Moreover, it is well-known for antifouling properties towards flavonoid's oxidation [163]. The CV and DPV were used for the analysis of the interaction of the hCNs targets with the CB-WS<sub>2</sub>/AuNPs-CT sensor surface. Their DPV results showed individual detection of CF, SP, and CM, while simultaneous detection of CF, SP, and CM generated three oxidation peaks at three different potentials (110 mV, 330 mV, and 490 mV). The data were analyzed by following polyphenol (PC) antioxidant capacity series to discriminate the three oxidation peaks. For example, (i) CF has a higher antioxidant capacity due to its ortho di-phenols structure and was oxidized at the lowest potential (110 mV). (ii) SP has an Intermediate antioxidant capacity with monophenols with a 4-hydroxy-3,5-dimethoxy structure, was oxidized at the intermediate potential (330 mV) and (iii) CM has the lowest antioxidant capacity among the three phenols with monophenols structure and was oxidized at the highest potential (490 mV). The results of this study were in line with earlier literature [164,165] that found that the antioxidant capacity series of polyphenols follows the trend of *o*-diphenols > methoxy-substitute monophenols > monophenols. The sensor showed a good limit of detection of 0.1 μmol L<sup>-1</sup>, 0.4 μmol L<sup>-1</sup>, and 0.4 μmol L<sup>-1</sup> for detection of CF, SP, and CM, respectively. It is worth mentioning here that this sensor has long-term stability. In a controlled condition, for the first 2 months, the response of the sensor decreased to 95%, however, it remained stable for the next 4 months (the sensor response was about 94%). It also successfully demonstrated simultaneous determination of CF, SP, and CM in a food sample with good precision (RSD ≤ 4%, *n* = 3). A different study reported the integration of WS<sub>2</sub> nanosheets with SPE for coccidiostat drug (roxarsone) determination that is widely used in poultry farming [166]. The roxarsone electro-reduction on the WS<sub>2</sub>/SPE electrode was concluded as an irreversible process, where the NO<sub>2</sub> was reduced to NH-OH (as shown in Figure 9), accompanied by a reduction peak potential at -0.64 V. The high current response has also been observed to be higher than electro-reduction roxarsone on bare SPE. Good catalytic performance and porous properties of WS<sub>2</sub> nanosheets could be the contributing key factors for the high current response. In a concentration-dependent experiment, the reduction peak of roxarsone increased successfully with the roxarsone concentration and showed an extremely good linear response in the range of 0.05 to 489.3 μM. LOD of this sensor was 0.03 μM. The sensor was also implemented for the determination of roxarsone in real meat samples, demonstrating accuracy of 96.29% and 112.5% in chicken extract and pork extract, respectively.

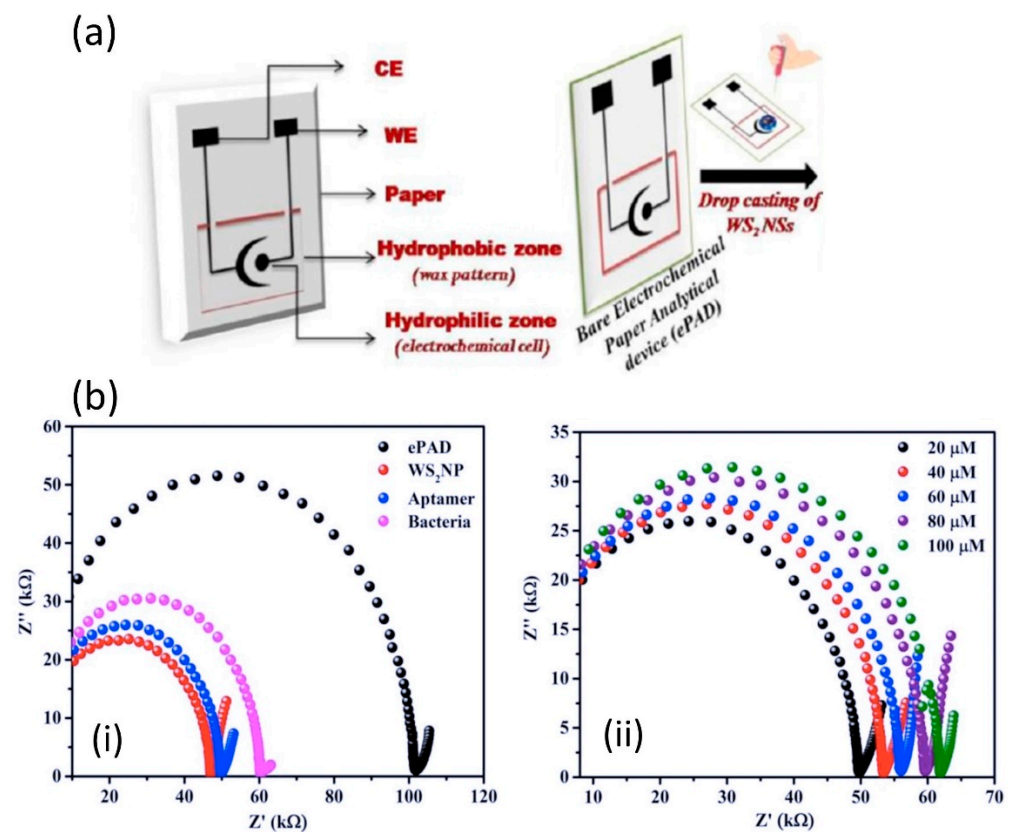


**Figure 8.** (a) Fabrication of screen-printed sensor on paper-based substrate is also well-known as paper-based analytical device (ePAD) and (b-i) Nyquist plot of bare ePAD, ePAD/WS<sub>2</sub>NS, after immobilization with aptamer and after immobilization with bacteria, (b-ii) Nyquist plot of detection bacteria at different concentration ranging from 20  $\mu$ M to 100  $\mu$ M. Reprinted with permission from [161]. Copyright 2021 MDPI. Authors licensed under a Creative Commons Attribution (CC BY) license.

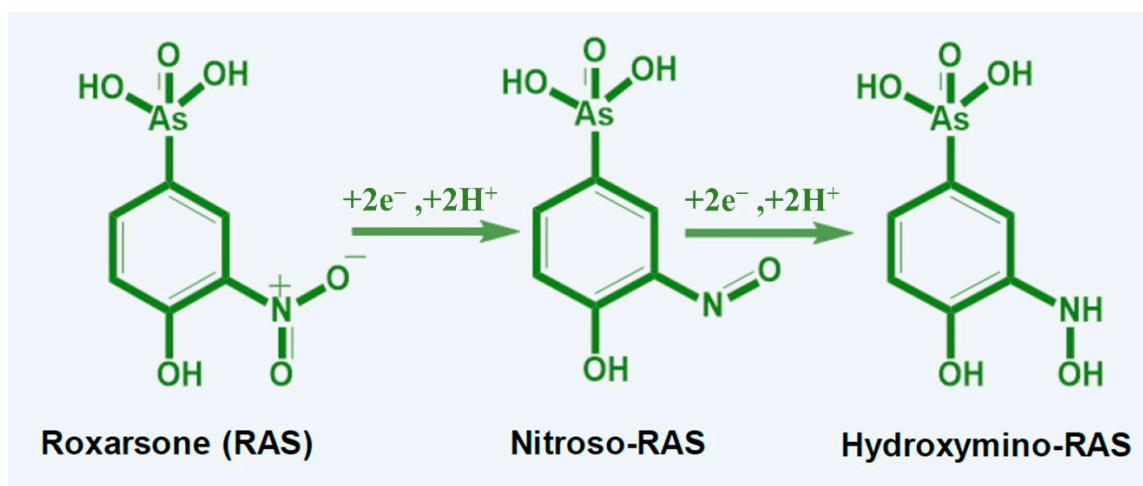


**Figure 9.** An illustration of electrocatalytic reaction mechanism of toxic roxarsone on the WS<sub>2</sub>-based SPE electrode sensor. Reprinted with permission from [167]. Copyright 2019 Elsevier.

## 5. MXenes

MXenes are a new class of two-dimensional material that has been proven to be valuable in various electronic fields, including biosensors, since its discovery in 2011 by Naguib et al. [168]. MXenes material is based on transition metal carbides and nitrides with

a chemical formula of  $M_{n+1}X_nT_x$ , where M represents a transition metal, X is an element of carbon or nitrogen, and  $T_x$  is denoted as termination on the surface of the outmost transition metal layers. The MXenes elements and four typical structures of MXenes materials are shown in Figure 10. Over the years, various MXenes have been demonstrated in literatures, however, only  $Ti_3C_2$  and  $Ti_2C$  are widely used in electronic applications. The discovery of MXenes materials about ten years ago opened another door of opportunity for sensing technology. MXenes offers high electrical conductivity ( $15\ 100\ S\ cm^{-1}$ ) owing to the metal component in its structure [169]. Essentially, MXenes have a negatively charged surface that mostly comprises hydroxyl (-OH), fluorine (-F), and oxygen (-O) groups [170]. These functional groups on MXene's surface are attributed to chemicals used during MXene's synthesizing process. Under those circumstances, this negatively charged surface can provide favorable reaction sites for positively charged molecules, for instance, heavy metal ions such as aluminum ( $Al^{3+}$ ), silver ( $Ag^+$ ), and copper ( $Cu^+$ ). Besides that, MXene's work functions are tunable by controlling electron density. On that account, with appropriate terminal groups, MXene's surface can be exploited for sensing certain analytes [171].

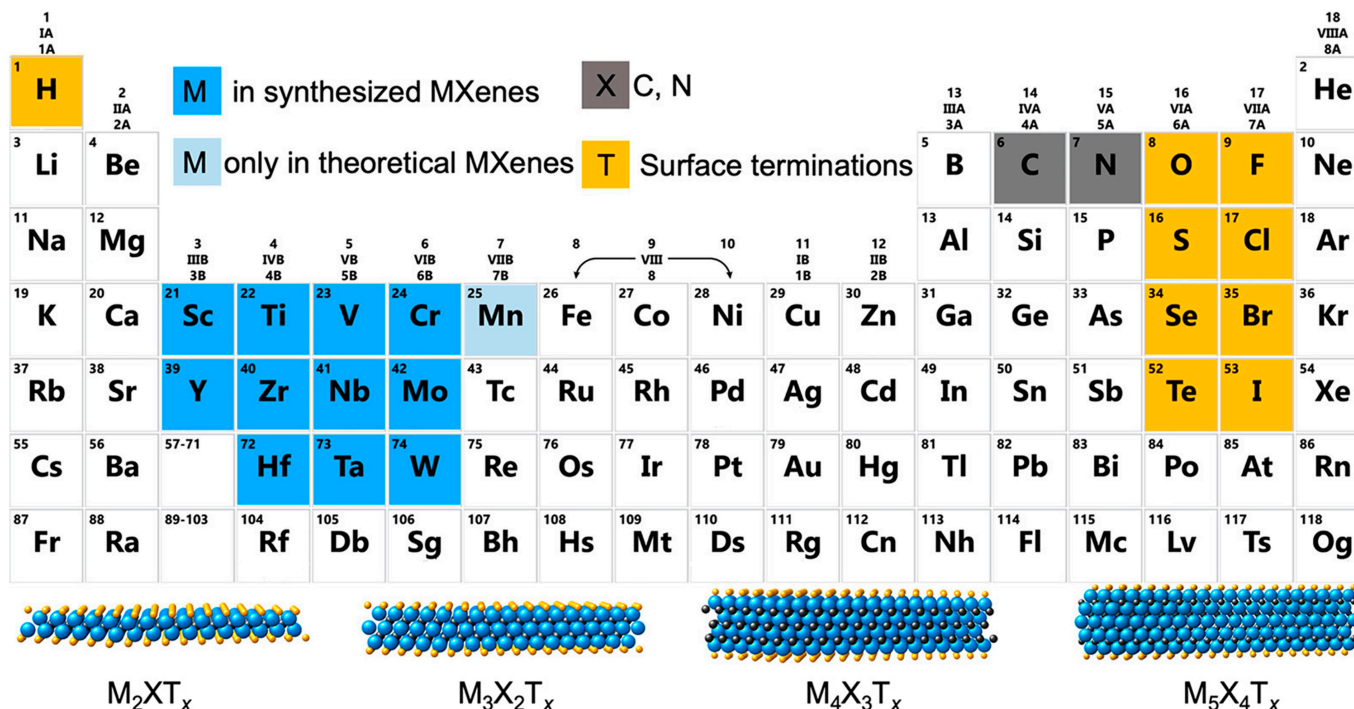


**Figure 10.** Periodic table presenting elements that are used in MXenes' composition. At the bottom are illustrations of four typical MXene structures. Reprinted (adapted) with permission from [172]. Copyright 2021 American Chemical Society.

The unstable nature of enzymes has restricted the use of enzymes in any sensor application. Immobilization of enzymes on substrate surfaces typically results in decreased enzyme activity and impaired efficiency [173]. Significant driving factors for the reduction in enzyme activity include binding procedure, diminished availability of enzyme molecules within substrate pores, or slowly diffusing substrate molecules. These factors are together known as mass transfer effect. Recently, Wu et al. [174] capitalized on MXenes material to develop a stable enzyme-based electrochemical sensor for detection of the D-2-hydroxyglutaric acid (D2HG) in serum and urine. *Ralstonia solanacearum* (*RsD2HGDH*) enzyme, used in this work as an ultrasensitive sensing element, was co-immobilized with methylene blue (MB) on  $Ti_2C_3$  MXenes sheet and further drop-cast onto the AuSPE with the help of chitosan. The research group reported that the stability of the *RsD2HGDH* enzyme was maintained even after 60 h immobilized on the MXenes surface. It is plausible that the *RsD2HGDH* benefited from the abundant functional groups of the MXenes Ih provided a

favorable environment for its immobilization. Research findings by Liu et al. also point towards functional groups that interact with the enzyme through weak interactions could stabilize the native structure while retaining the enzyme activity [175]. The detection of the sensor was based on the electron transfer between *RsD2HGDH* and the gold electrode. In the presence of D2HG, *RsD2HGDH* will be catalyzed and generate electrons. These electrons were shuttled through the MB mediator to the sensor electrode. The prepared *RsD2HGDH*-MXenes-AuSPE biosensor showed detection of D2HG in the range of 0.5 to 120  $\mu\text{M}$ , with LOD of 0.1  $\mu\text{M}$ . The sensitivity of the biosensor was 22.26  $\mu\text{A mM}^{-1} \text{cm}^{-2}$ . The authors claimed that their AuSPE sensor gave better performance compared to the commercial D2HG assays kit, with LOD of 10  $\mu\text{M}$  and essentially needs controlled temperature when operating. Nevertheless, this sensor system suffers a drawback from the use of the mediator. They reported that the oxygens were competing with the mediators in some experiments, while the stability and biological toxicity of the mediators need further investigation. Therefore, to overcome the problem with mediator, further studies on new D2HGDH that can bypass the mediated electron transfer is essential.

A valuable advantage of SPE sensors is that their sensing element can be printed directly on a substrate, consequently, remove complexity of the sensor device's fabrication. Moreover, direct printable sensing materials can minimize sensor variation with controlled film thickness and hold great potential for mass production. Saleh et al. and his research group developed water-based MXenes ink and inkjet-printed MXenes film on freestanding poly(3,4-ethylenedioxythiophene):polystyrene sulfonate (PEDOT:PSS), that is suitable for wearable printed sensors [176]. Of note, the MXenes material has shown outstanding hydrophilicity and biocompatibility with biological tissue, making it an ideal candidate for a skin-contact sensor. Owing to PEDOT's conductive properties, the entire MXenes sensor fabrication required only a single printing step. The metallic connection underneath the MXENEs electrode was unnecessary. This is because PEDOT allowed for a conducting, metal-like contact point to external acquisition system. The prepared MXenes electrode was tested for recording electrocardiography (ECG) signals from skin. Generally, commercial Ag/AgCl gel-type electrodes have been used to measure such signals. Therefore, it is reasonable to compare the performance of the MXenes electrode with the commercial Ag/AgCl electrode for ECG signal recordings. Their findings showed that the impedance between MXenes and the human skin was lower than the impedance of the Ag/AgCl electrode, suggesting conformability of the MXenes film electrode on human skin. Moreover, both MXenes and Ag/AgCl electrodes produced a similar ECG signal profile with comparable signal-to-noise ratio ( $\text{SNR}_{\text{MXene}} = 7.1$ ,  $\text{SNR}_{\text{Ag/AgCl}} = 6.7$ ). They further carried out other experiments to demonstrate the potential of their printed MXenes electrode for biosensor applications. In the first biosensor experiment, they attempted to detect  $\text{Na}^+$  cations in sweat.  $\text{Na}^+$  ion-sensitive membranes (ISM) were drop-casted on top of MXenes' printed electrode, and the sensitivity of the  $\text{Na}^+$  was evaluated by recording its open circuit potential (OCP) vs. Ag/AgCl while varying concentration of  $\text{Na}^+$ . They reported that the ISM/MXenes sensors' response was linear to the concentration of the  $\text{Na}^+$  with a slope of 40 mV/decade. Their second MXenes biosensor experiment involved the integration of interferon gamma ( $\text{IFN}\gamma$ ) antibody on MXenes electrode. Similar to the previous experiment, the  $\text{IFN}\gamma$  antibody functionalization on MXene's electrode was done by drop-casting method. Physical absorption of the antibody allowed for binding with MXene's surface; therefore, an immunosensor was successfully constructed and used for cytokine proteins detection in different concentrations. The sensitivity of the immunosensor was reported to be 3.9 mV per decade. Saleh's study of MXenes as skin conformable electronics is considered to be one of the most important; however, it suffers from a lack of analysis in real samples.

Zhang and co-workers developed a voltametric sensor using screen-printed modified with MXenes for detection of AC and INZ [177]. A SPE surface was functionalized through drop-coating method of MXenes solution. Detection of INZ and AC in 0.1M  $\text{H}_2\text{SO}_4$  supporting electrolyte on the MXenes/SPE gave a well-defined DPV current signal without

overlapping with each other, thereby suggesting that this sensor was potentially used for simultaneous detection. The operating range of this sensor for AC detection was 0.25 to 2000  $\mu\text{M}$ , while the range for INZ detection was 0.1 to 4.6 mM. Both detections demonstrated linear sensing responses proportionate to concentrations. The LODs of this sensor were 0.048  $\mu\text{M}$  and 0.064 mM for AC and INZ detection, respectively. Moreover, these sensor performances were comparable to or even better than those of other works in the literature that used different sensing platforms. Zhang et al. concluded that their remarkable sensing performances of this sensor was attributed to MXenes material. Firstly,  $\text{Ti}_3\text{C}_2\text{T}_x$  MXenes is titanium-rich material. It not only provides robust carbon support but also allows for an effective conductive channel for electrons. Secondly, MXenes favors many active sites' exposure and facilitates faster electron transfer during the electrocatalytic process owing to its accordion-like layered structure. Lastly,  $\text{Ti}_3\text{C}_2\text{T}_x$  MXenes is generally a negatively charged surface with -F, -OH and =O functional groups; therefore, it is beneficial to the aggregation of positively charged analytes such as INZ.

Integration of an electrochemical sensor with a microfluidic system has certainly paved a new pathway for high sensitivity sensing with automation and miniaturization features. For example, Liu et al. implemented MXenes-modified SPE with a microfluidic system for a direct and continuous multicomponent analysis of whole blood. The microfluidic system was comprised of four layers, as shown in Figure 11, where the top layer had a channel for blood flow and the second layer, which was made up of dialysis membrane, allowed for small molecules to penetrate (size molecule < 1000 Da), while the third layer was designed with a flow channel for isotonic solution and a detection chamber. The analytes in blood were dialyzed into the channel at this layer and gathered in detection chamber. Lastly, at the very bottom layer, the electrochemical electrode was positioned for sensing purposes. For the sensing electrode part, the authors carefully designed the sensing matrices on SPE. To increase sensing surface area and enhance electrocatalytic activity, the SPE sensing surface was coated with MXenes, followed by the addition of methylene blue (MB) to adjust the background signal and aid measurement stability. Finally, the authors immobilized urease with the aid of glutaraldehyde on the MXene surface to generate a specific signal for urea analysis. This novel biosensing system demonstrated detection of creatinine (Cre) with LOD of  $1.2 \times 10^{-6}$  M in the linear range of  $10\text{--}400 \times 10^{-6}$  M. While the detection of uric acid (UA) gave current responses that were not so linear with the UA concentration, it is still acceptable as a general logarithmic trend. The logarithmic relation between current response and concentration was in the range of  $30\text{--}500 \times 10^{-6}$  M with LOD of  $5 \times 10^{-6}$  M. With the same sensing system, the authors performed the determination of urea. They reported that the electrical response displayed linear relation with urea concentration in the range of  $0\text{--}3 \times 10^{-3}$  M. The same sensing system exhibited excellent performance in the quantification of those tricomponents in real whole blood sample analysis. The recoveries of the novel biosensing system were 90.41–98.28% (UA), 90.16–99.82% (urea), and 83.59–95.66% (Cre).

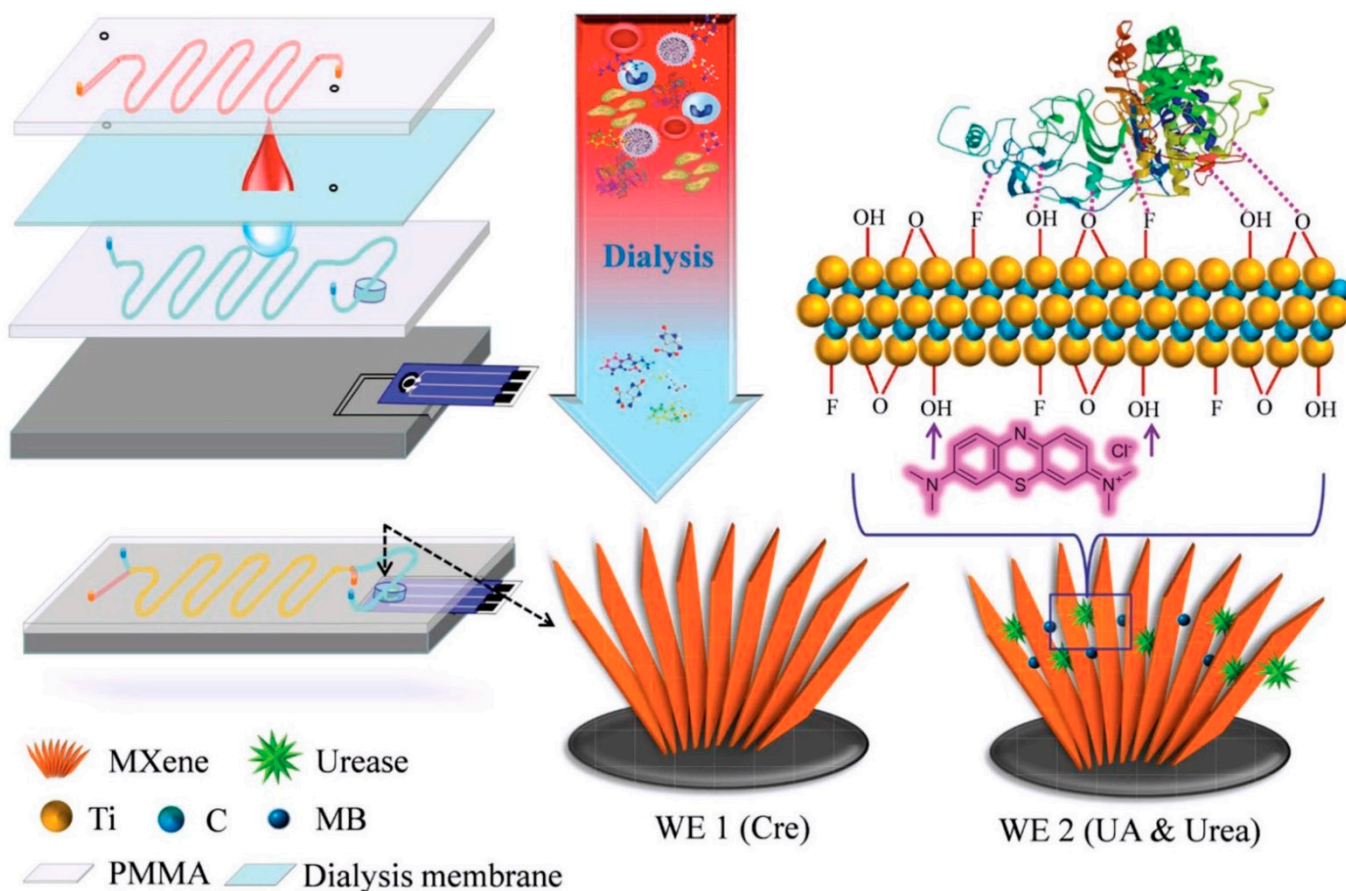


**Figure 11.** Structure of a microfluidic system with MXenes/MB/urea SPE for whole blood detection. Reprinted with permission from reference [178]. Copyright 2019 John Wiley and Sons.

## 6. Hexagonal Boron-Nitride (h-BN)

h-BN is one of the emerging materials in the 2D material class with promising potential for electronics applications. The h-BN nanosheet has a dense honeycomb layered structure analogous to that of graphite, which contains  $sp^2$  hybridized B-N bonds. In a h-BN bulk structure, a few single h-BN layers are stacked together through Van der Waals interaction, which boron and nitrogen atoms are placed alternately as shown in Figure 12a, while in every single layer of h-BN, B and N are linked by a strong covalent bond in a  $sp^2$ -hybridized honeycomb lattice (Figure 12b) [179]. Among the other 2D materials, hexagonal boron-nitride is an unpopular material for electronic applications due to initial reports of it being non-conductive [180,181]. Despite the fact that h-BN is reported as a non-conductive material, Ferrari et al. provide a comprehensive review of its use in electroanalytical sensing platforms [36]. Herein, we will specifically cover the topic of h-BN as material for sensing on printable electrode platform.

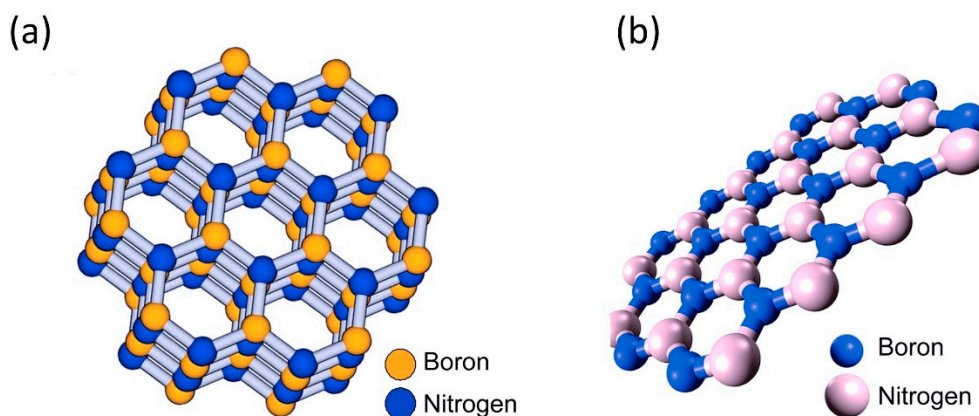


**Figure 12.** Illustration of the atomic structure of hexagonal boron-nitride (a) in a bulk structure, (b) in a monolayer structure. Reprinted from [179], with the permission of AIP Publishing.

Yue et al. constructed a biosensor on SPE using h-BN conjugated with silver nanoparticles (AgNPs) as a probe for the detection of scopoletin [182]. Before being drop-cast on a SPE WE, AgNPs were first deposited onto an h-BN layer to form a nanocomposite. The AgNPs on hBN were found to increase the active site numbers, accelerate the electron transfer, and expand sensor surface area. Through CV analysis, the hBN/AgNPs/SPE sensor exhibited high electrocatalytic activity towards scopoletin, as its oxidation peak current increased significantly compared to scopoletin on bare SPE sensor. Further, the sensitivity of the modified SPE towards scopoletin was analyzed with DPV signals, which were recorded through scopoletin oxidation at concentrations ranging from 2  $\mu\text{M}$  to 0.45 mM, yielding LOD of 0.89  $\mu\text{M}$  with SNR of 3. The research group also reported success in the determination of scopoletin in *Atractylodes macrocephala* herb. The average concentration of scopoletin found in the herb was 5.478  $\mu\text{M}$ . This value has been verified with HPLC Agilent 1100 to confirm the accuracy of the hBN/AgNPs/SPE sensor. A study by Öndes et al. proves that biological recognition element can be directly tethered on h-BN nanosheet for detection of ovarian cancer [183]. The surface electrode of SPE was modified with boron nitride nanosheets, followed with immobilization of anti CA125 antibody on the nanosheet for probing purposes. Previous research has shown that the BN surface has natural affinity for protein bindings, which the lysine unit of the protein has strong attraction towards the boron atom on the BN nanosheet [184]. Therefore, the protein can attach to BN nanosheets through absorption without the need for coupling agent. Öndes et al. recorded significant decreased in CV redox current when analyzed BN on SPE. This result is attributed to the insulator characteristic of BN, whose covalent layer of boron and nitrogen atom localizes free electrons. Interestingly, after immobilization of the antibody, the redox current magnitude increased. This is a rather unexpected result. This result contradicted other previous studies in which the immunosensor DPV readings decreased with increasing antigen concentration [185–188]. The researchers described the cause of the DPV's decreased peak current with increasing antigen concentration as being due to electron transferability between the electrode surface and redox probe being hindered by antigen-antibody bindings. In corroboration with increasing redox current, the authors of the presented study presumed that the antibody molecules might have entered between BN layers, thus increasing the number of transfer electrons. Their hypothesis seems to be consistent with other research, which found that molecules and ions can be presented in the intra-layer spacing between the BN sheets [189]. Through DPV, the established immunosensor displayed 1.18 U/mL LOD using ferro/ferri cyanide as a redox probe. The immunosensor also showed good detection in a linear range of 5–100 U. To assess its practicality in real-world applications, the immunosensor was tested in artificial human serum spiked with 20 and 50 U/mL of CA125. The DPV measurement was carried out for this experiment, and they reported average relative recoveries of 98.13% and 101.22%

for 20 and 50 U/mL CA125, respectively. Kokulnathan's research team capitalized on the bismuth oxide and hexagonal boron nitride ( $\text{Bi}_2\text{O}_3/\text{h-BN}$ ) nanocomposites heterostructure to construct a disposable electrochemical sensor for detection of flutamide, which is commonly used in the treatment of prostatic cancer [190]. They modified a carbon SPE with the  $\text{Bi}_2\text{O}_3/\text{h-BN}$  nanocomposite through dripping method, followed by drying process in an oven. The strong interaction between 2D hBN and bismuth oxide modifies the physical and electronic properties of the nanocomposite. The modified electrode was reported to have become rough, which gives it favorable characteristics for electrochemical sensing. Rough surfaces provide a larger surface area and thereby enhance sensing efficiency. The electrochemical detection of flutamide was established through the existence of free carriers in the nanocomposite heterojunction. The LOD value of 9.0 nM was achieved with good linear ranges of 0.04–87  $\mu\text{M}$  obtained by the DPV response method.

## 7. Conclusions

The advantages of low cost and high reliability have drawn significant research attention to printed electrochemical sensors. They have long been developed with various types of electrode materials such as carbon, gold, platinum, and so forth that enable electrocatalytic reactions for high sensitivity sensors. We have surveyed recent advances in non-carbon 2D materials integration with printed electrochemical sensors and discussed key developments of the sensor from the perspective of materials. Within the past five years, TMDC's  $\text{MoS}_2$  material has shown rapid advancement as a material for surface modification on the printed sensor. The popularity of  $\text{MoS}_2$  in printed electrochemical sensor applications stems from its versatile features.  $\text{MoS}_2$  makes a very ideal candidate for sensing material owing to its extraordinary electrical properties. Being physically almost similar to its counterpart graphene, but featuring tunable bandgap properties have certainly attracted much attentions to study  $\text{MoS}_2$  as a sensing material. Despite the fact that  $\text{MoS}_2$  materials have shown continuous advancement in the sensor field, TMDC materials are generally still in their infancy compared to long established graphene and silicon materials. Thus, it could be explained why the other TMDC materials ( $\text{MoSe}_2$ ,  $\text{WS}_2$ , etc.) are still scarcely explored for printed electrochemical sensors. At a future time, we can anticipate many other TMDC compounds being capitalized as sensing materials. Similar to TMDC, MXenes is also a new 2D material that was introduced in 2011. MXenes have recently been gaining popularity as a preferred material for sensors owing to its high conductivity. However, MXenes require more time to establish in the sensor field as it is facing challenges at the synthesis level, such as easy aggregation and poor stability in oxygen atmosphere. In the case of hBN, it was the least popular as sensing material because of its insulator property. Having said that, hBN is really advantageous when combined with the other materials or elements as a sensing layer.

Let us now consider the challenges that are facing us in this printed sensor field. Despite the impressive achievements that have been made in this field, printed sensors are still having difficulties in a few areas and crucially need to be addressed. (1) To fabricate a very robust and sensitive sensing platform with low a detection limit and a wide dynamic range for application in real sample analysis still remain as the primary challenge in the sensors field. The complex matrices in real samples (e.g., urine, blood, human serum, lake water) will cause serious interferences, and the lower concentration of the target analytes will result in difficulty for direct determination. Due to competition between the target analytes and other molecules in the matrices to form bonds with the recognition sites on the sensing surface area, the sensor's sensitivity is possibly lower in real samples. Furthermore, the interference in the matrices may also lead to false positive results. Choosing high performance electrode and sensing element materials is prominent to achieve high sensitivity sensor response, especially in complex matrices. Sensor integration with microfluidic systems that are equipped with filtering features can also help to filter out unwanted molecules, resulting in a more sensitive response. (2) Most of the studies reviewed in this article employed drop-casting as their primary method for sensor surface functionalization

and modification. This technique, however, has raised concerns about the robustness and reproducibility of sensors. In reality, drop-casting for surface functionalization is not a very straightforward technique. The execution of the technique is very simple; however, it involves a complex process that is controlled by particle interactions, molecular packing constraints, together with kinetic and thermodynamic factors. In addition, as we discussed in the introduction part of this article, the drop-cast technique has the tendency to produce a coffee ring effect, where modifier particles are not evenly distributed on the sensing surface. Moreover, due to the sparse coverage, it cannot be guaranteed that all the modifier particles are in electrical contact with the substrate or are not aggregated. Consequently, these two factors can affect the signal reproducibility of the sensor. For real sample analysis, it is important to have a batch fabrication of sensors that will permit similar and consistent results. Therefore, future research might focus on the incorporation of modifier material in the electrode ink to fabricate the printed sensor. The major advantages of this method are that the sensor's reproducibility is possible owing to evenly distributed recognition sites on the sensor surface, and the sensor signal can be improved. (3) In the healthcare field, flexible printed electrochemical sensors are usually associated with wearable monitoring systems. Despite the massive progress that has been made in wearable electrochemical sensor systems, the integration of power sources and the ability to communicate via wireless network remains a great challenge. Further research on the development of a power source that can scavenge power from the body via biokinetics or body heat is vital to enabling the application of printed electrochemical sensors as real-time wearable monitoring devices.

**Author Contributions:** Conceptualization, S.F.; writing—original draft preparation, S.F., S.A.S. and M.S.; writing—review and editing, S.F., J.C.J. and M.S.; visualization, K.A. and M.S., data curation, K.A., S.A.S. and J.C.J.; supervision, M.S. and A.A.M.; project administration, A.A.M. and H.K.; funding acquisition, S.F. and M.S. All authors have read and agreed to the published version of the manuscript.

**Funding:** This research was funded by Biogenes Research Aptamer Grant, grant number "304.PCEDEC.6050470.B139" and Top Down Research University Grant Universiti Sains Malaysia with grant number "1001/PCEDEC/870050".

**Institutional Review Board Statement:** Not applicable.

**Informed Consent Statement:** Not applicable.

**Data Availability Statement:** Not applicable.

**Acknowledgments:** A part of this study was supported by project of Creation of Life Innovation Materials for Interdisciplinary and International Researcher Development (MEXT), and Kawarada Laboratory, Waseda University, Tokyo (Japan). The authors would like to express gratitude to Biogenes Technologies Sdn. Bhd. for their contribution towards CEDEC, USM, and INOR, USM.

**Conflicts of Interest:** The authors declare no conflict of interest.

## References

1. Mohamed, H.M. Screen-printed disposable electrodes: Pharmaceutical applications and recent developments. *TrAC Trends Anal. Chem.* **2016**, *82*, 1–11. [[CrossRef](#)]
2. Engel, L.; Tarantik, K.R.; Pannek, C.; Prades, J.D.; Wöllenstein, J. Screen-printable Colorimetric Sensors for the Monitoring of Toxic Gases in Ambient Air. In Proceedings of the 2019 IEEE International Conference on Flexible and Printable Sensors and Systems (FLEPS), Glasgow, UK, 8–10 July 2019; pp. 3–5. [[CrossRef](#)]
3. Parate, K.; Pola, C.C.; Rangnekar, S.V.; Mendivelso-Perez, D.L.; Smith, E.A.; Hersam, M.C.; Gomes, C.L.; Claussen, J.C. Aerosol-jet-printed graphene electrochemical histamine sensors for food safety monitoring. *2D Mater.* **2020**, *7*, 0334002. [[CrossRef](#)]
4. Ogończyk, D.; Tymecki, Ł.; Wyzkiewicz, I.; Koncki, R.; Głab, S. Screen-printed disposable urease-based biosensors for inhibitive detection of heavy metal ions. *Sens. Actuators B Chem.* **2005**, *106*, 450–454. [[CrossRef](#)]
5. Lu, R.; Haider, M.R.; Gardner, S.; Alexander, J.I.D.; Massoud, Y. A Paper-Based Inkjet-Printed Graphene Sensor for Breathing-Flow Monitoring. *IEEE Sens. Lett.* **2019**, *3*, 6000104. [[CrossRef](#)]
6. Li, J.P.; Peng, T.Z.; Fang, C. Screen-printable sol-gel ceramic carbon composite pH sensor with a receptor zeolite. *Anal. Chim. Acta* **2002**, *455*, 53–60. [[CrossRef](#)]

7. Chen, Z.; Patel, R.; Berry, J.; Keyes, C.; Satterfield, C.; Simmons, C.; Neeson, A.; Cao, X.; Wu, Q. Development of Screen-Printable Nafion Dispersion for Electrochemical Sensor. *Appl. Sci.* **2022**, *12*, 6533. [[CrossRef](#)]
8. Sekitani, T.; Nakajima, H.; Maeda, H.; Fukushima, T.; Aida, T.; Hata, K.; Someya, T. Stretchable active-matrix organic light-emitting diode display using printable elastic conductors. *Nat. Mater.* **2009**, *8*, 494–499. [[CrossRef](#)]
9. Sonoyama, T.; Ito, M.; Seki, S.; Miyashita, S.; Xia, S.; Brooks, J.; Cheon, K.-O.; Kwong, R.C.; Inbasekaran, M.; Brown, J.J. Ink-jet-printable phosphorescent organic light-emitting-diode devices. *J. Soc. Inf. Disp.* **2008**, *16*, 1229–1236. [[CrossRef](#)]
10. Lin, Y.; Gao, Y.; Fang, F.; Fan, Z. Recent progress on printable power supply devices and systems with nanomaterials. *Nano Res.* **2018**, *11*, 3065–3087. [[CrossRef](#)]
11. Song, J.; Xu, L.; Li, J.; Xue, J.; Dong, Y.; Li, X.; Zeng, H. Monolayer and Few-Layer All-Inorganic Perovskites as a New Family of Two-Dimensional Semiconductors for Printable Optoelectronic Devices. *Adv. Mater.* **2016**, *28*, 4861–4869. [[CrossRef](#)]
12. Zhao, J.; Lu, H.; Zhao, X.; Malyi, O.I.; Peng, J.; Lu, C.; Li, X.; Zhang, Y.; Zeng, Z.; Xing, G.; et al. Printable Ink Design towards Customizable Miniaturized Energy Storage Devices. *ACS Mater. Lett.* **2020**, *2*, 1041–1056. [[CrossRef](#)]
13. Amin, E.M.; Bhuiyan, M.S.; Karmakar, N.C.; Winther-Jensen, B. Development of a low cost printable chipless RFID humidity sensor. *IEEE Sens. J.* **2014**, *14*, 140–149. [[CrossRef](#)]
14. Oluwasanya, P.W.; Samad, Y.A.; Ochipinti, L.G. Printable sensors for Nitrogen dioxide and Ammonia sensing at room temperature. In Proceedings of the 2019 IEEE International Conference on Flexible and Printable Sensors and Systems (FLEPS), Glasgow, UK, 8–10 July 2019; pp. 19–21. [[CrossRef](#)]
15. Carrasquilla, C.; Little, J.R.L.; Li, Y.; Brennan, J.D. Patterned paper sensors printed with long-chain DNA aptamers. *Chem.—Eur. J.* **2015**, *21*, 7369–7373. [[CrossRef](#)] [[PubMed](#)]
16. Qiu, X.; Chiechi, R.C. Printable logic circuits comprising self-assembled protein complexes. *Nat. Commun.* **2022**, *13*, 2312. [[CrossRef](#)]
17. Baeg, K.J.; Khim, D.; Kim, D.Y.; Jung, S.W.; Koo, J.B.; You, I.K.; Yan, H.; Facchetti, A.; Noh, Y.Y. High speeds complementary integrated circuits fabricated with all-printed polymeric semiconductors. *J. Polym. Sci. Part B Polym. Phys.* **2011**, *49*, 62–67. [[CrossRef](#)]
18. Hayasaka, K.; Matsui, H.; Takeda, Y.; Shiwaku, R.; Tanaka, Y.; Shiba, T.; Kumaki, D.; Tokito, S. Compact Organic Complementary D-Type Flip-Flop Circuits Fabricated with Inkjet Printing. *Adv. Electron. Mater.* **2017**, *3*, 1700208. [[CrossRef](#)]
19. Jang, Y.; Hartarto Tambunan, I.; Tak, H.; Dat Nguyen, V.; Kang, T.; Byun, D. Non-contact printing of high aspect ratio Ag electrodes for polycrystalline silicon solar cell with electrohydrodynamic jet printing. *Appl. Phys. Lett.* **2013**, *102*, 123901. [[CrossRef](#)]
20. Inui, T.; Mandampambal, R.; Araki, T.; Abbel, R.; Koga, H.; Nogi, M.; Suganuma, K. Laser-induced forward transfer of high-viscosity silver precursor ink for non-contact printed electronics. *RSC Adv.* **2015**, *5*, 77942–77947. [[CrossRef](#)]
21. Mondal, K.; McMurtrey, M.D. Present status of the functional advanced micro-, nano-printings—A mini review. *Mater. Today Chem.* **2020**, *17*, 100328. [[CrossRef](#)]
22. Secor, E.B. Principles of Aerosol Jet Printing. *Flex. Print. Electron.* **2018**, *3*, 035002. [[CrossRef](#)]
23. Sherigara, B.S.; Kutner, W.; D’Souza, F. Electrocatalytic properties and sensor applications of fullerenes and carbon nanotubes. *Electroanalysis* **2003**, *15*, 753–772. [[CrossRef](#)]
24. Roy, S.; Soin, N.; Bajpai, R.; Misra, D.S.; McLaughlin, J.A.; Roy, S.S. Graphene oxide for electrochemical sensing applications. *J. Chem. Chem.* **2011**, *21*, 14725–14731. [[CrossRef](#)]
25. Wu, S.; He, Q.; Tan, C.; Wang, Y.; Zhang, H. Graphene-based electrochemical sensors. *Small* **2013**, *9*, 1160–1172. [[CrossRef](#)] [[PubMed](#)]
26. Tung, T.T.; Nine, M.J.; Krebsz, M.; Pasinszki, T.; Coghlan, C.J.; Tran, D.N.H.; Losic, D. Recent Advances in Sensing Applications of Graphene Assemblies and Their Composites. *Adv. Funct. Mater.* **2017**, *27*, 1702891. [[CrossRef](#)]
27. Pei, Y.; Zhang, X.; Hui, Z.; Zhou, J.; Huang, X.; Sun, G.; Huang, W. Ti3C2TXMXene for Sensing Applications: Recent Progress, Design Principles, and Future Perspectives. *ACS Nano* **2021**, *15*, 3996–4017. [[CrossRef](#)] [[PubMed](#)]
28. Jayabal, S.; Wu, J.; Chen, J.; Geng, D.; Meng, X. Metallic 1T-MoS2 nanosheets and their composite materials: Preparation, properties and emerging applications. *Mater. Today Energy* **2018**, *10*, 264–279. [[CrossRef](#)]
29. Chhowalla, M.; Shin, H.S.; Eda, G.; Li, L.J.; Loh, K.P.; Zhang, H. The chemistry of two-dimensional layered transition metal dichalcogenide nanosheets. *Nat. Chem.* **2013**, *5*, 263–275. [[CrossRef](#)]
30. Wang, N.; Yang, G.; Wang, H.; Yan, C.; Sun, R.; Wong, C.P. A universal method for large-yield and high-concentration exfoliation of two-dimensional hexagonal boron nitride nanosheets. *Mater. Today* **2019**, *27*, 33–42. [[CrossRef](#)]
31. Ma, C.; Ma, M.G.; Si, C.; Ji, X.X.; Wan, P. Flexible MXene-Based Composites for Wearable Devices. *Adv. Funct. Mater.* **2021**, *31*, 2009524. [[CrossRef](#)]
32. Korotcenkov, G. Black phosphorus-new nanostructured material for humidity sensors: Achievements and limitations. *Sensors* **2019**, *19*, 1010. [[CrossRef](#)]
33. Jin, W.; Zhang, W.; Gao, Y.; Liang, G.; Gu, A.; Yuan, L. Surface functionalization of hexagonal boron nitride and its effect on the structure and performance of composites. *Appl. Surf. Sci.* **2013**, *270*, 561–571. [[CrossRef](#)]
34. Kalambate, P.K.; Gadhari, N.S.; Li, X.; Rao, Z.; Navale, S.T.; Shen, Y.; Patil, V.R.; Huang, Y. Recent advances in MXene-based electrochemical sensors and biosensors. *TrAC Trends Anal. Chem.* **2019**, *120*, 115643. [[CrossRef](#)]

35. Jiang, F.; Zhao, W.S.; Zhang, J. Mini-review: Recent progress in the development of MoSe<sub>2</sub> based chemical sensors and biosensors. *Microelectron. Eng.* **2020**, *225*, 111279. [[CrossRef](#)]
36. García-Miranda Ferrari, A.; Rowley-Neale, S.J.; Banks, C.E. Recent advances in 2D hexagonal boron nitride (2D-hBN) applied as the basis of electrochemical sensing platforms. *Anal. Bioanal. Chem.* **2021**, *413*, 663–672. [[CrossRef](#)]
37. Mohammadniaei, M.; Nguyen, H.V.; Van Tieu, M.; Lee, M.H. 2D materials in development of electrochemical point-of-care cancer screening devices. *Micromachines* **2019**, *10*, 662. [[CrossRef](#)]
38. Anichini, C.; Czepa, W.; Pakulski, D.; Aliprandi, A.; Ciesielski, A.; Samorì, P. Chemical sensing with 2D materials. *Chem. Soc. Rev.* **2018**, *47*, 4860–4908. [[CrossRef](#)]
39. Ambaye, A.D.; Kefeni, K.K.; Mishra, S.B.; Nxumalo, E.N.; Ntsendwana, B. Recent developments in nanotechnology-based printing electrode systems for electrochemical sensors. *Talanta* **2021**, *225*, 121951. [[CrossRef](#)]
40. Cancelliere, R.; Cianciaruso, M.; Carbone, K.; Micheli, L. Biochar: A Sustainable Alternative in the Development of Electrochemical Printed Platforms. *Chemosensors* **2022**, *10*, 344. [[CrossRef](#)]
41. Alrammouz, R.; Podlecki, J.; Abboud, P.; Sorli, B.; Habchi, R. A review on flexible gas sensors: From materials to devices. *Sens. Actuators A Phys.* **2018**, *284*, 209–231. [[CrossRef](#)]
42. Fioravanti, A.; Carotta, M.C. Year 2020: A snapshot of the last progress in flexible printed gas sensors. *Appl. Sci.* **2020**, *10*, 1741. [[CrossRef](#)]
43. Delipinar, T.; Shafique, A.; Gohar, M.S.; Yapici, M.K. Fabrication and Materials Integration of Flexible Humidity Sensors for Emerging Applications. *ACS Omega* **2021**, *6*, 8744–8753. [[CrossRef](#)] [[PubMed](#)]
44. Barmpakos, D.; Kaltsas, G. A review on humidity, temperature and strain printed sensors—Current trends and future perspectives. *Sensors* **2021**, *21*, 739. [[CrossRef](#)] [[PubMed](#)]
45. Alatraktchi, F.A.Z.; Noori, J.S.; Tanev, G.P.; Mortensen, J.; Dimaki, M.; Johansen, H.K.; Madsen, J.; Molin, S.; Svendsen, W.E. Paper-based sensors for rapid detection of virulence factor produced by *Pseudomonas aeruginosa*. *PLoS ONE* **2018**, *13*, e0194157. [[CrossRef](#)] [[PubMed](#)]
46. Jabari, E.; Ahmed, F.; Liravi, F.; Secor, E.B.; Lin, L.; Toyserkani, E. 2D printing of graphene: A review. *2D Mater.* **2019**, *6*, 042004. [[CrossRef](#)]
47. Goh, G.L.; Agarwala, S.; Yeong, W.Y. Aerosol-Jet-Printed Preferentially Aligned Carbon Nanotube Twin-Lines for Printed Electronics. *ACS Appl. Mater. Interfaces* **2019**, *11*, 43719–43730. [[CrossRef](#)]
48. Vestergaard, M.C.; Kerman, K.; Hsing, I.M.; Tamiya, E. *Nanobiosensors and Nanobioanalyses*; Springer: New York, NY, USA, 2015; pp. 1–379. ISBN 9784431551904. [[CrossRef](#)]
49. Arduini, F.; Di Nardo, F.; Amine, A.; Micheli, L.; Palleschi, G.; Moscone, D. Carbon Black-Modified Screen-Printed Electrodes as Electroanalytical Tools. *Electroanalysis* **2012**, *24*, 743–751. [[CrossRef](#)]
50. Vicentini, F.C.; Ravanini, A.E.; Figueiredo-Filho, L.C.S.; Iniesta, J.; Banks, C.E.; Fatibello-Filho, O. Imparting improvements in electrochemical sensors: Evaluation of different carbon blacks that give rise to significant improvement in the performance of electroanalytical sensing platforms. *Electrochim. Acta* **2015**, *157*, 125–133. [[CrossRef](#)]
51. Cinti, S.; Neagu, D.; Carbone, M.; Cacciotti, I.; Moscone, D.; Arduini, F. Novel Carbon Black-Cobalt Phthalocyanine Nanocomposite as Sensing Platform to Detect Organophosphorus Pollutants at Screen-Printed Electrode. *Electrochim. Acta* **2016**, *188*, 574–581. [[CrossRef](#)]
52. Kunpatee, K.; Traipop, S.; Chailapakul, O.; Chuanuwatanakul, S. Simultaneous determination of ascorbic acid, dopamine, and uric acid using graphene quantum dots/ionic liquid modified screen-printed carbon electrode. *Sens. Actuators B Chem.* **2020**, *314*, 128059. [[CrossRef](#)]
53. Obaje, E.A.; Cummins, G.; Schulze, H.; Mahmood, S.; Desmulliez, M.P.Y.; Bachmann, T.T. Carbon screen-printed electrodes on ceramic substrates for label-free molecular detection of antibiotic resistance. *J. Interdiscip. Nanomed.* **2016**, *1*, 93–109. [[CrossRef](#)]
54. Bain, C.D.; Troughton, E.B.; Tao, Y.T.; Evall, J.; Whitesides, G.M.; Nuzzo, R.G. Formation of Monolayer Films by the Spontaneous Assembly of Organic Thiols from Solution onto Gold. *J. Am. Chem. Soc.* **1989**, *111*, 321–335. [[CrossRef](#)]
55. Li, Y.; Mao, Y.; Xiao, C.; Xu, X.; Li, X. Flexible pH sensor based on a conductive PANI membrane for pH monitoring. *RSC Adv.* **2019**, *10*, 21–28. [[CrossRef](#)] [[PubMed](#)]
56. Windmiller, J.R.; Bandodkar, A.J.; Parkhomovsky, S.; Wang, J. Stamp transfer electrodes for electrochemical sensing on non-planar and oversized surfaces. *Analyst* **2012**, *137*, 1570–1575. [[CrossRef](#)] [[PubMed](#)]
57. Liu, X.; Lillehoj, P.B. Embroidered electrochemical sensors for biomolecular detection. *Lab A Chip* **2016**, *16*, 2093–2098. [[CrossRef](#)]
58. Mishra, R.K.; Barfidokht, A.; Karajic, A.; Sempionatto, J.R.; Wang, J.; Wang, J. Wearable potentiometric tattoo biosensor for on-body detection of G-type nerve agents simulants. *Sens. Actuators B Chem.* **2018**, *273*, 966–972. [[CrossRef](#)]
59. Sardini, E.; Serpelloni, M.; Tonello, S. Printed electrochemical biosensors: Opportunities and metrological challenges. *Biosensors* **2020**, *10*, 166. [[CrossRef](#)]
60. Rocchitta, G.; Spanu, A.; Babudieri, S.; Latte, G.; Madeddu, G.; Galleri, G.; Nuvoli, S.; Bagella, P.; Demartis, M.I.; Fiore, V.; et al. Enzyme biosensors for biomedical applications: Strategies for safeguarding analytical performances in biological fluids. *Sensors* **2016**, *16*, 780. [[CrossRef](#)]
61. Li, H.; Liu, X.; Li, L.; Mu, X.; Genov, R.; Mason, A.J. CMOS electrochemical instrumentation for biosensor microsystems: A review. *Sensors* **2017**, *17*, 74. [[CrossRef](#)]

62. Zhang, X.; Huang, X.; Xu, Y.; Wang, X.; Guo, Z.; Huang, X.; Li, Z.; Shi, J.; Zou, X. Single-step electrochemical sensing of ppt-level lead in leaf vegetables based on peroxidase-mimicking metal-organic framework. *Biosens. Bioelectron.* **2020**, *168*, 112544. [[CrossRef](#)]
63. Bond, A.M.; Compton, R.G.; Fiedler, D.A.; Inzelt, G.; Kahlert, H.; Lohse, H.; Lovric, M.; Lovric, S.K.; Marken, F.; Neudeck, A.; et al. *Electroanalytical Methods; Guide to Experiments and Applications 2nd, Revised and Extended Edition*; Springer: Berlin, Germany, 2009; ISBN 9783642029141.
64. Kaliyaraj Selva Kumar, A.; Zhang, Y.; Li, D.; Compton, R.G. A mini-review: How reliable is the drop casting technique? *Electrochem. Commun.* **2020**, *121*, 106867. [[CrossRef](#)]
65. Deegan, R.D.; Bakajin, O.; Dupont, T.F. Deegan Nat 1997. *Nature* **1997**, *389*, 827–829. [[CrossRef](#)]
66. Park, J.; Moon, J. Control of colloidal particle deposit patterns within picoliter droplets ejected by ink-jet printing. *Langmuir* **2006**, *22*, 3506–3513. [[CrossRef](#)] [[PubMed](#)]
67. Kuang, M.; Wang, L.; Song, Y. Controllable Printing Droplets for High-Resolution Patterns. *Adv. Mater.* **2014**, *26*, 6950–6958. [[CrossRef](#)] [[PubMed](#)]
68. Friederich, A.; Binder, J.R.; Bauer, W. Rheological control of the coffee stain effect for inkjet printing of ceramics. *J. Am. Ceram. Soc.* **2013**, *96*, 2093–2099. [[CrossRef](#)]
69. Arduini, F.; Cinti, S.; Mazzaracchio, V.; Scognamiglio, V.; Amine, A.; Moscone, D. Carbon black as an outstanding and affordable nanomaterial for electrochemical (bio)sensor design. *Biosens. Bioelectron.* **2020**, *156*, 112033. [[CrossRef](#)] [[PubMed](#)]
70. Wisitsoraat, A.; Mensing, J.P.; Karuwan, C.; Sriprachuabwong, C.; Jaruwongrungrsee, K.; Phokharatkul, D.; Daniels, T.M.; Liewhiran, C.; Tuantranont, A. Printed organo-functionalized graphene for biosensing applications. *Biosens. Bioelectron.* **2017**, *87*, 7–17. [[CrossRef](#)]
71. Camargo, J.R.; Orzari, L.O.; Araújo, D.A.G.; de Oliveira, P.R.; Kalinke, C.; Rocha, D.P.; Luiz dos Santos, A.; Takeuchi, R.M.; Munoz, R.A.A.; Bonacin, J.A.; et al. Development of conductive inks for electrochemical sensors and biosensors. *Microchem. J.* **2021**, *164*, 105998. [[CrossRef](#)]
72. Jiang, D.; Chu, Z.; Peng, J.; Jin, W. Screen-printed biosensor chips with Prussian blue nanocubes for the detection of physiological analytes. *Sens. Actuators B Chem.* **2016**, *228*, 679–687. [[CrossRef](#)]
73. Mass, M.; Veiga, L.S.; Garate, O.; Longinotti, G.; Moya, A.; Ramón, E.; Villa, R.; Ybarra, G.; Gabriel, G. Fully inkjet-printed biosensors fabricated with a highly stable ink based on carbon nanotubes and enzyme-functionalized nanoparticles. *Nanomaterials* **2021**, *11*, 1645. [[CrossRef](#)]
74. Wang, H.S.; Pan, Q.X.; Wang, G.X. A biosensor based on immobilization of horseradish peroxidase in chitosan matrix cross-linked with glyoxal for amperometric determination of hydrogen peroxide. *Sensors* **2005**, *5*, 266–276. [[CrossRef](#)]
75. Rodrigues, R.C.; Ortiz, C.; Berenguer-Murcia, Á.; Torres, R.; Fernández-Lafuente, R. Modifying enzyme activity and selectivity by immobilization. *Chem. Soc. Rev.* **2013**, *42*, 6290–6307. [[CrossRef](#)]
76. Hoarau, M.; Badiéyan, S.; Marsh, E.N.G. Immobilized enzymes: Understanding enzyme-surface interactions at the molecular level. *Org. Biomol. Chem.* **2017**, *15*, 9539–9551. [[CrossRef](#)]
77. Bardpho, C.; Rattanarat, P.; Siangproh, W.; Chailapakul, O. Ultra-high performance liquid chromatographic determination of antioxidants in teas using inkjet-printed graphene-polyaniline electrode. *Talanta* **2016**, *148*, 673–679. [[CrossRef](#)] [[PubMed](#)]
78. Teengam, P.; Siangproh, W.; Tuantranont, A.; Henry, C.S.; Vilaivan, T.; Chailapakul, O. Electrochemical paper-based peptide nucleic acid biosensor for detecting human papillomavirus. *Anal. Chim. Acta* **2017**, *952*, 32–40. [[CrossRef](#)]
79. Kit-Anan, W.; Olarnwanich, A.; Sriprachuabwong, C.; Karuwan, C.; Tuantranont, A.; Wisitsoraat, A.; Srituravanich, W.; Pimpin, A. Disposable paper-based electrochemical sensor utilizing inkjet-printed Polyaniline modified screen-printed carbon electrode for Ascorbic acid detection. *J. Electroanal. Chem.* **2012**, *685*, 72–78. [[CrossRef](#)]
80. Chen, K.; Chou, W.; Liu, L.; Cui, Y.; Xue, P.; Jia, M. Electrochemical sensors fabricated by electrospinning technology: An overview. *Sensors* **2019**, *19*, 3676. [[CrossRef](#)] [[PubMed](#)]
81. Kavadiya, S.; Biswas, P. Electrospray deposition of biomolecules: Applications, challenges, and recommendations. *J. Aerosol Sci.* **2018**, *125*, 182–207. [[CrossRef](#)]
82. Cioffi, N.; Colaianni, L.; Ieva, E.; Pilolli, R.; Ditaranto, N.; Angione, M.D.; Cotrone, S.; Buchholt, K.; Spetz, A.L.; Sabbatini, L.; et al. Electrosynthesis and characterization of gold nanoparticles for electronic capacitance sensing of pollutants. *Electrochim. Acta* **2011**, *56*, 3713–3720. [[CrossRef](#)]
83. Scavetta, E.; Casagrande, A.; Gualandi, I.; Tonelli, D. Analytical performances of Ni LDH films electrochemically deposited on Pt surfaces: Phenol and glucose detection. *J. Electroanal. Chem.* **2014**, *722–723*, 15–22. [[CrossRef](#)]
84. Domínguez-Domínguez, S.; Arias-Pardilla, J.; Berenguer-Murcia, Á.; Morallón, E.; Cazorla-Amorós, D. Electrochemical deposition of platinum nanoparticles on different carbon supports and conducting polymers. *J. Appl. Electrochem.* **2008**, *38*, 259–268. [[CrossRef](#)]
85. Rodríguez-Sánchez, L.; Blanco, M.C.; López-Quintela, M.A. Electrochemical synthesis of silver nanoparticles. *Electrochem. Commun.* **2006**, *8*, 227–230. [[CrossRef](#)]
86. Tu, D.; He, Y.; Rong, Y.; Wang, Y.; Li, G. Disposable L-lactate biosensor based on a screen-printed carbon electrode enhanced by graphene. *Meas. Sci. Technol.* **2016**, *27*, 045108. [[CrossRef](#)]

87. Hondred, J.A.; Breger, J.C.; Alves, N.J.; Trammell, S.A.; Walper, S.A.; Medintz, I.L.; Claussen, J.C. Printed Graphene Electrochemical Biosensors Fabricated by Inkjet Maskless Lithography for Rapid and Sensitive Detection of Organophosphates. *ACS Appl. Mater. Interfaces* **2018**, *10*, 11125–11134. [[CrossRef](#)] [[PubMed](#)]
88. Maghsoudi, A.S.; Hassani, S.; Akmal, M.R.; Ganjali, M.R.; Mirnia, K.; Norouzi, P.; Abdollahi, M. An electrochemical aptasensor platform based on flower-like gold microstructure-modified screen-printed carbon electrode for detection of serpin A12 as a type 2 diabetes biomarker. *Int. J. Nanomed.* **2020**, *15*, 2219–2230. [[CrossRef](#)]
89. Traiwatcharanon, P.; Siriwatcharapiboon, W.; Jongprateep, O.; Wongchoosuk, C. Electrochemical paraquat sensor based on lead oxide nanoparticles. *RSC Adv.* **2022**, *12*, 16079–16092. [[CrossRef](#)]
90. Zhang, C.J.; McKeon, L.; Kremer, M.P.; Park, S.H.; Ronan, O.; Seral-Ascaso, A.; Barwich, S.; Coileáin, C.; McEvoy, N.; Nerl, H.C.; et al. Additive-free MXene inks and direct printing of micro-supercapacitors. *Nat. Commun.* **2019**, *10*, 1795. [[CrossRef](#)]
91. Pavithra, C.L.P.; Sarada, B.V.; Rajulapati, K.V.; Rao, T.N.; Sundararajan, G. A new electrochemical approach for the synthesis of copper-graphene nanocomposite foils with high hardness. *Sci. Rep.* **2014**, *4*, 4049. [[CrossRef](#)]
92. Falina, S.; Syamsul, M.; Rhaffor, N.A.; Sal Hamid, S.; Mohamed Zain, K.A.; Abd Manaf, A.; Kawarada, H. Ten years progress of electrical detection of heavy metal ions (Hmis) using various field-effect transistor (fet) nanosensors: A review. *Biosensors* **2021**, *11*, 478. [[CrossRef](#)]
93. Zhu, S.; Gong, L.; Xie, J.; Gu, Z.; Zhao, Y. Design, Synthesis, and Surface Modification of Materials Based on Transition-Metal Dichalcogenides for Biomedical Applications. *Small Methods* **2017**, *1*, 1700220. [[CrossRef](#)]
94. Monga, D.; Sharma, S.; Shetti, N.P.; Basu, S.; Reddy, K.R.; Aminabhavi, T.M. Advances in transition metal dichalcogenide-based two-dimensional nanomaterials. *Mater. Today Chem.* **2021**, *19*, 100399. [[CrossRef](#)]
95. Li, Z.; Wong, S.L. Functionalization of 2D transition metal dichalcogenides for biomedical applications. *Mater. Sci. Eng. C* **2017**, *70*, 1095–1106. [[CrossRef](#)] [[PubMed](#)]
96. Zhu, C.; Zeng, Z.; Li, H.; Li, F.; Fan, C.; Zhang, H. Single-layer MoS<sub>2</sub>-based nanoprobe for homogeneous detection of biomolecules. *J. Am. Chem. Soc.* **2013**, *135*, 5998–6001. [[CrossRef](#)] [[PubMed](#)]
97. Cheng, L.; Liu, J.; Gu, X.; Gong, H.; Shi, X.; Liu, T.; Wang, C.; Wang, X.; Liu, G.; Xing, H.; et al. PEGylated WS<sub>2</sub> nanosheets as a multifunctional theranostic agent for in vivo dual-modal CT/photoacoustic imaging guided photothermal therapy. *Adv. Mater.* **2014**, *26*, 1886–1893. [[CrossRef](#)] [[PubMed](#)]
98. Jin, C.; Ma, E.Y.; Karni, O.; Regan, E.C.; Wang, F.; Heinz, T.F. Ultrafast dynamics in van der Waals heterostructures. *Nat. Nanotechnol.* **2018**, *13*, 994–1003. [[CrossRef](#)]
99. Wang, Q.H.; Kalantar-Zadeh, K.; Kis, A.; Coleman, J.N.; Strano, M.S. Electronics and optoelectronics of two-dimensional transition metal dichalcogenides. *Nat. Nanotechnol.* **2012**, *7*, 699–712. [[CrossRef](#)]
100. Radisavljevic, B.; Radenovic, A.; Brivio, J.; Giacometti, V.; Kis, A. Single-layer MoS<sub>2</sub> transistors. *Nat. Nanotechnol.* **2011**, *6*, 147–150. [[CrossRef](#)]
101. Mann, J.; Ma, Q.; Odenthal, P.M.; Isarraraz, M.; Le, D.; Preciado, E.; Barroso, D.; Yamaguchi, K.; Von Son Palacio, G.; Nguyen, A.; et al. 2-Dimensional transition metal dichalcogenides with tunable direct band gaps: MoS<sub>2</sub>(1-x)Se<sub>2x</sub> monolayers. *Adv. Mater.* **2014**, *26*, 1399–1404. [[CrossRef](#)]
102. Pavličková, M.; Lorencová, L.; Hatala, M.; Kováč, M.; Tkáč, J.; Gemeiner, P. Facile fabrication of screen-printed MoS<sub>2</sub> electrodes for electrochemical sensing of dopamine. *Sci. Rep.* **2022**, *12*, 11900. [[CrossRef](#)]
103. Asefifeyzabadi, N.; Alkhalidi, R.; Qamar, A.Z.; Pater, A.A.; Patwardhan, M.; Gagnon, K.T.; Talapatra, S.; Shamsi, M.H. Label-free Electrochemical Detection of CGG Repeats on Inkjet PrinTable 2D Layers of MoS<sub>2</sub>. *ACS Appl. Mater. Interfaces* **2020**, *12*, 52156–52165. [[CrossRef](#)]
104. Chu, Y.; Cai, B.; Ma, Y.; Zhao, M.; Ye, Z.; Huang, J. Highly sensitive electrochemical detection of circulating tumor DNA based on thin-layer MoS<sub>2</sub>/graphene composites. *RSC Adv.* **2016**, *6*, 22673–22678. [[CrossRef](#)]
105. Loo, A.H.; Bonanni, A.; Ambrosi, A.; Pumera, M. Molybdenum disulfide (MoS<sub>2</sub>) nanoflakes as inherently electroactive labels for DNA hybridization detection. *Nanoscale* **2014**, *6*, 11971–11975. [[CrossRef](#)] [[PubMed](#)]
106. Zribi, R.; Maalej, R.; Messina, E.; Gillibert, R.; Donato, M.G.; Maragò, O.M.; Gucciardi, P.G.; Leonardi, S.G.; Neri, G. Exfoliated 2D-MoS<sub>2</sub> nanosheets on carbon and gold screen printed electrodes for enzyme-free electrochemical sensing of tyrosine. *Sens. Actuators B Chem.* **2020**, *303*, 127229. [[CrossRef](#)]
107. Chia, X.; Eng, A.Y.S.; Ambrosi, A.; Tan, S.M.; Pumera, M. Electrochemistry of Nanostructured Layered Transition-Metal Dichalcogenides. *Chem. Rev.* **2015**, *115*, 11941–11966. [[CrossRef](#)] [[PubMed](#)]
108. Zribi, R.; Maalej, R.; Gillibert, R.; Donato, M.G.; Gucciardi, P.G.; Leonardi, S.G.; Neri, G. Simultaneous and selective determination of dopamine and tyrosine in the presence of uric acid with 2D-MoS<sub>2</sub> nanosheets modified screen-printed carbon electrodes. *FlatChem* **2020**, *24*, 100187. [[CrossRef](#)]
109. Liang, W.; Ren, H.; Li, Y.; Qiu, H.; Ye, B.C. A robust electrochemical sensing based on bimetallic metal-organic framework mediated Mo<sub>2</sub>C for simultaneous determination of acetaminophen and isoniazid. *Anal. Chim. Acta* **2020**, *1136*, 99–105. [[CrossRef](#)]
110. Yan, H.; Xiao, H.; Xie, Q.; Liu, J.; Sun, L.; Zhou, Y.; Zhang, Y.; Chao, L.; Chen, C.; Yao, S. Simultaneous electroanalysis of isoniazid and uric acid at poly(sulfosalicylic acid)/electroreduced carboxylated graphene modified glassy carbon electrode. *Sens. Actuators B Chem.* **2015**, *207*, 167–176. [[CrossRef](#)]

111. Tseng, T.W.; Chen, T.W.; Chen, S.M.; Kokulnathan, T.; Ahmed, F.; Hasan, P.M.Z.; Bilgrami, A.L.; Kumar, S. Construction of strontium phosphate/graphitic-carbon nitride: A flexible and disposable strip for acetaminophen detection. *J. Hazard. Mater.* **2021**, *410*, 124542. [[CrossRef](#)]
112. Neethipathi, D.K.; Ganguly, P.; Beniwal, A.; Scott, M.; Bass, A.; Dahiya, R. MoS<sub>2</sub> modified screen printed carbon electrode based flexible sensor for detection of Copper. In Proceedings of the 2022 IEEE International Conference on Flexible and Printable Sensors and Systems (FLEPS), Vienna, Austria, 10–13 July 2022; IEEE: Piscataway, NJ, USA, 2022; pp. 1–4. [[CrossRef](#)]
113. Di Tinno, A.; Cancelliere, R.; Mantegazza, P.; Cataldo, A.; Paddubskaya, A.; Ferrigno, L.; Kuzhir, P.; Maksimenko, S.; Shuba, M.; Maffucci, A.; et al. Sensitive Detection of Industrial Pollutants Using Modified Electrochemical Platforms. *Nanomaterials* **2022**, *12*, 1779. [[CrossRef](#)]
114. Tajik, S.; Dourandish, Z.; Nejad, F.G.; Aghaei Afshar, A.; Beitollahi, H. Voltammetric Determination of Isoniazid in the Presence of Acetaminophen Utilizing MoS<sub>2</sub>-Nanosheet-Modified Screen-Printed Electrode. *Micromachines* **2022**, *13*, 369. [[CrossRef](#)]
115. Demir, N.; Atacan, K.; Ozmen, M.; Bas, S.Z. Design of a new electrochemical sensing system based on MoS<sub>2</sub>-TiO<sub>2</sub>/reduced graphene oxide nanocomposite for the detection of paracetamol. *New J. Chem.* **2020**, *44*, 11759–11767. [[CrossRef](#)]
116. Zhang, H.; Loh, K.P.; Sow, C.H.; Gu, H.; Su, X.; Huang, C.; Chen, Z.K. Surface modification studies of edge-oriented molybdenum sulfide nanosheets. *Langmuir* **2004**, *20*, 6914–6920. [[CrossRef](#)]
117. Shu, Y.; Zhang, W.; Cai, H.; Yang, Y.; Yu, X.; Gao, Q. Expanding the interlayers of molybdenum disulfide toward the highly sensitive sensing of hydrogen peroxide. *Nanoscale* **2019**, *11*, 6644–6653. [[CrossRef](#)] [[PubMed](#)]
118. Shetti, N.P.; Malode, S.J.; Nayak, D.S.; Aminabhavi, T.M.; Reddy, K.R. Nanostructured silver doped TiO<sub>2</sub>/CNTs hybrid as an efficient electrochemical sensor for detection of anti-inflammatory drug, cetirizine. *Microchem. J.* **2019**, *150*, 104124. [[CrossRef](#)]
119. Nazarpour, S.; Hajian, R.; Sabzvari, M.H. A novel nanocomposite electrochemical sensor based on green synthesis of reduced graphene oxide/gold nanoparticles modified screen printed electrode for determination of tryptophan using response surface methodology approach. *Microchem. J.* **2020**, *154*, 104634. [[CrossRef](#)]
120. Gui, J.C.; Han, L.; Du, C.X.; Yu, X.N.; Hu, K.; Li, L.H. An efficient label-free immunosensor based on ce-MoS<sub>2</sub>/AgNR composites and screen-printed electrodes for PSA detection. *J. Solid State Electrochem.* **2021**, *25*, 973–982. [[CrossRef](#)]
121. Sadeghi, M.; Jahanshahi, M.; Javadian, H. Highly sensitive biosensor for detection of DNA nucleobases: Enhanced electrochemical sensing based on polyaniline/single-layer MoS<sub>2</sub> nanosheets nanocomposite modified carbon paste electrode. *Microchem. J.* **2020**, *152*, 104315. [[CrossRef](#)]
122. Zhang, C.; Ping, J.; Ye, Z.; Ying, Y. Two-dimensional nanocomposite-based electrochemical sensor for rapid determination of trans-resveratrol. *Sci. Total Environ.* **2020**, *742*, 140351. [[CrossRef](#)]
123. Acerce, M.; Voiry, D.; Chhowalla, M. Metallic 1T phase MoS<sub>2</sub> nanosheets as supercapacitor electrode materials. *Nat. Nanotechnol.* **2015**, *10*, 313–318. [[CrossRef](#)]
124. Du, P.; Zhu, Y.; Zhang, J.; Xu, D.; Peng, W.; Zhang, G.; Zhang, F.; Fan, X. Metallic 1T phase MoS<sub>2</sub> nanosheets as a highly efficient co-catalyst for the photocatalytic hydrogen evolution of CdS nanorods. *RSC Adv.* **2016**, *6*, 74394–74399. [[CrossRef](#)]
125. Dai, J.; Yao, L.; Gao, X.; Bai, S.; Chen, X.; Li, L.; Song, J.; Yang, H. To achieve ultrasensitive electrochemical detection of mercury ions employing metallic 1T-MoS<sub>2</sub> nanosheets. *Electrochim. Acta* **2020**, *355*, 136800. [[CrossRef](#)]
126. Shi, S.; Sun, Z.; Hu, Y.H. Synthesis, stabilization and applications of 2-dimensional 1T metallic MoS<sub>2</sub>. *J. Mater. Chem. A* **2018**, *6*, 23932–23977. [[CrossRef](#)]
127. Sim, D.M.; Han, H.J.; Yim, S.; Choi, M.J.; Jeon, J.; Jung, Y.S. Long-Term Stable 2H-MoS<sub>2</sub> Dispersion: Critical Role of Solvent for Simultaneous Phase Restoration and Surface Functionalization of Liquid-Exfoliated MoS<sub>2</sub>. *ACS Omega* **2017**, *2*, 4678–4687. [[CrossRef](#)] [[PubMed](#)]
128. Fan, X.L.; Yang, Y.; Xiao, P.; Lau, W.M. Site-specific catalytic activity in exfoliated MoS<sub>2</sub> single-layer polytypes for hydrogen evolution: Basal plane and edges. *J. Mater. Chem. A* **2014**, *2*, 20545–20551. [[CrossRef](#)]
129. Er, E.; Erk, N. Construction of a sensitive electrochemical sensor based on 1T-MoS<sub>2</sub> nanosheets decorated with shape-controlled gold nanostructures for the voltammetric determination of doxorubicin. *Microchim. Acta* **2020**, *187*, 223. [[CrossRef](#)]
130. Vacek, J.; Havran, L.; Fojta, M. Ex situ voltammetry and chronopotentiometry of doxorubicin at a pyrolytic graphite electrode: Redox and catalytic properties and analytical applications. *Electroanalysis* **2009**, *21*, 2139–2144. [[CrossRef](#)]
131. Ganguly, A.; Benson, J.; Papakonstantinou, P. Sensitive chronocoulometric detection of miRNA at screen-printed electrodes modified by gold-decorated MoS<sub>2</sub> nanosheets. *ACS Appl. Bio Mater.* **2018**, *1*, 1184–1194. [[CrossRef](#)] [[PubMed](#)]
132. Steel, A.B.; Herne, T.M.; Tarlov, M.J. Electrochemical quantitation of DNA immobilized on gold. *Anal. Chem.* **1998**, *70*, 4670–4677. [[CrossRef](#)]
133. Singhal, C.; Khanuja, M.; Chaudhary, N.; Pundir, C.S.; Narang, J. Detection of chikungunya virus DNA using two-dimensional MoS<sub>2</sub> nanosheets based disposable biosensor. *Sci. Rep.* **2018**, *8*, 7734. [[CrossRef](#)]
134. Raveendran, M.; Andrade, A.F.B.; Gonzalez-Rodriguez, J. Selective and sensitive electrochemical DNA biosensor for the detection of bacillus anthracis. *Int. J. Electrochem. Sci.* **2016**, *11*, 763–776.
135. Arévalo, B.; Blázquez-García, M.; Valverde, A.; Serafín, V.; Montero-Calle, A.; Solís-Fernández, G.; Barderas, R.; Campuzano, S.; Yáñez-Sedeño, P.; Pingarrón, J.M. Binary MoS<sub>2</sub> nanostructures as nanocarriers for amplification in multiplexed electrochemical immunosensing: Simultaneous determination of B cell activation factor and proliferation-induced signal immunity-related cytokines. *Microchim. Acta* **2022**, *189*, 143. [[CrossRef](#)]

136. Villa-Manso, A.M.; Revenga-Parra, M.; Vera-Hidalgo, M.; Vázquez Sulleiro, M.; Pérez, E.M.; Lorenzo, E.; Pariente, F. 2D MoS<sub>2</sub> nanosheets and hematein complexes deposited on screen-printed graphene electrodes as an efficient electrocatalytic sensor for detecting hydrazine. *Sens. Actuators B Chem.* **2021**, *345*, 130385. [[CrossRef](#)]
137. Selvam, S.P.; Chinnadaiyala, S.R.; Cho, S. Electrochemical nanobiosensor for early detection of rheumatoid arthritis biomarker: Anti-cyclic citrullinated peptide antibodies based on polyaniline (PANI)/MoS<sub>2</sub>-modified screen-printed electrode with PANI-Au nanomatrix-based signal amplification. *Sens. Actuators B Chem.* **2021**, *333*, 129570. [[CrossRef](#)]
138. Hamami, M.; Bouaziz, M.; Raouafi, N.; Bendounan, A.; Korri-Youssoufi, H. MoS<sub>2</sub>/ppy nanocomposite as a transducer for electrochemical aptasensor of ampicillin in river water. *Biosensors* **2021**, *11*, 311. [[CrossRef](#)] [[PubMed](#)]
139. Ariyanta, H.A.; Ivandini, T.A.; Yulizar, Y. Poly(methyl orange)-modified NiO/MoS<sub>2</sub>/SPCE for a non-enzymatic detection of cholesterol. *FlatChem* **2021**, *29*, 100285. [[CrossRef](#)]
140. Gobalu, K.; Vasudevan, M.; Gopinath, S.C.B.; Perumal, V.; Ovinis, M. Molybdenum disulphide/cellulose acetate nanofiber composite on screen printed electrodes for detecting cardiac troponin by electrical impedance spectroscopy. *Cellulose* **2021**, *28*, 5761–5774. [[CrossRef](#)]
141. Jiang, D.; Sheng, K.; Gui, G.; Jiang, H.; Liu, X.; Wang, L. A novel smartphone-based electrochemical cell sensor for evaluating the toxicity of heavy metal ions Cd<sup>2+</sup>, Hg<sup>2+</sup>, and Pb<sup>2+</sup> in rice. *Anal. Bioanal. Chem.* **2021**, *413*, 4277–4287. [[CrossRef](#)]
142. Vasudevan, M.; Tai, M.J.Y.; Perumal, V.; Gopinath, S.C.B.; Murthe, S.S.; Ovinis, M.; Mohamed, N.M.; Joshi, N. Cellulose acetate-MoS<sub>2</sub> nanopetal hybrid: A highly sensitive and selective electrochemical aptasensor of Troponin I for the early diagnosis of Acute Myocardial Infarction. *J. Taiwan Inst. Chem. Eng.* **2021**, *118*, 245–253. [[CrossRef](#)]
143. Singh, A.P.; Balayan, S.; Gupta, S.; Jain, U.; Sarin, R.K.; Chauhan, N. Detection of pesticide residues utilizing enzyme-electrode interface via nano-patterning of TiO<sub>2</sub> nanoparticles and molybdenum disulfide (MoS<sub>2</sub>) nanosheets. *Process Biochem.* **2021**, *108*, 185–193. [[CrossRef](#)]
144. Martínez-Periñán, E.; García-Mendiola, T.; Enebral-Romero, E.; del Caño, R.; Vera-Hidalgo, M.; Vázquez Sulleiro, M.; Navío, C.; Pariente, F.; Pérez, E.M.; Lorenzo, E. A MoS<sub>2</sub> platform and thionine-carbon nanodots for sensitive and selective detection of pathogens. *Biosens. Bioelectron.* **2021**, *189*, 113375. [[CrossRef](#)]
145. Li, X.; Zhang, M.; Hu, Y.; Xu, J.; Sun, D.; Hu, T.; Ni, Z. Screen-printed electrochemical biosensor based on a ternary Co@MoS<sub>2</sub>/rGO functionalized electrode for high-performance non-enzymatic glucose sensing. *Biomed. Microdevices* **2020**, *22*, 17. [[CrossRef](#)]
146. Della Pelle, F.; Rojas, D.; Scroccarello, A.; Del Carlo, M.; Ferraro, G.; Di Mattia, C.; Martuscelli, M.; Escarpa, A.; Compagnone, D. High-performance carbon black/molybdenum disulfide nanohybrid sensor for cocoa catechins determination using an extraction-free approach. *Sens. Actuators B Chem.* **2019**, *296*, 126651. [[CrossRef](#)]
147. Toh, R.J.; Mayorga-Martinez, C.C.; Sofer, Z.; Pumera, M. MoSe<sub>2</sub> Nanolabels for Electrochemical Immunoassays. *Anal. Chem.* **2016**, *88*, 12204–12209. [[CrossRef](#)] [[PubMed](#)]
148. Wang, W.; Dong, Y.; Xu, L.; Dong, W.; Niu, X.; Lei, Z. Combining Bimetallic-Alloy with Selenium Functionalized Carbon to Enhance Electrocatalytic Activity towards Glucose Oxidation. *Electrochim. Acta* **2017**, *244*, 16–25. [[CrossRef](#)]
149. Sakthivel, M.; Ramaraj, S.; Chen, S.M.; Dinesh, B.; Ramasamy, H.V.; Lee, Y.S. Entrapment of bimetallic CoFeSe<sub>2</sub> nanosphere on functionalized carbon nanofiber for selective and sensitive electrochemical detection of caffeic acid in wine samples. *Anal. Chim. Acta* **2018**, *1006*, 22–32. [[CrossRef](#)]
150. Luo, Z.; Zhou, J.; Wang, L.; Fang, G.; Pan, A.; Liang, S. Two-dimensional hybrid nanosheets of few layered MoSe<sub>2</sub> on reduced graphene oxide as anodes for long-cycle-life lithium-ion batteries. *J. Mater. Chem. A* **2016**, *4*, 15302–15308. [[CrossRef](#)]
151. Wiensch, J.D.; John, J.; Velazquez, J.M.; Torelli, D.A.; Pieterick, A.P.; McDowell, M.T.; Sun, K.; Zhao, X.; Brunschwig, B.S.; Lewis, N.S. Comparative Study in Acidic and Alkaline Media of the Effects of pH and Crystallinity on the Hydrogen-Evolution Reaction on MoS<sub>2</sub> and MoSe<sub>2</sub>. *ACS Energy Lett.* **2017**, *2*, 2234–2238. [[CrossRef](#)]
152. Chu, H.; Liu, X.; Liu, B.; Zhu, G.; Lei, W.; Du, H.; Liu, J.; Li, J.; Li, C.; Sun, C. Hexagonal 2H-MoSe<sub>2</sub> broad spectrum active photocatalyst for Cr(VI) reduction. *Sci. Rep.* **2016**, *6*, 35304. [[CrossRef](#)]
153. Luo, Y.; Wu, D.; Li, Z.; Li, X.; Wu, Y.; Feng, S.; Menon, C.; Chen, H.; Chu, P.K. Plasma functionalized MoSe<sub>2</sub> for efficient nonenzymatic sensing of hydrogen peroxide in ultra-wide pH range. *SmartMat* **2022**, *3*, 491–502. [[CrossRef](#)]
154. Qu, Y.; Medina, H.; Wang, S.W.; Wang, Y.C.; Chen, C.W.; Su, T.Y.; Manikandan, A.; Wang, K.; Shih, Y.C.; Chang, J.W.; et al. Wafer Scale Phase-Engineered 1T- and 2H-MoSe<sub>2</sub>/Mo Core-Shell 3D-Hierarchical Nanostructures toward Efficient Electrocatalytic Hydrogen Evolution Reaction. *Adv. Mater.* **2016**, *28*, 9831–9838. [[CrossRef](#)]
155. Ramaraj, S.; Sakthivel, M.; Chen, S.M.; Lou, B.S.; Ho, K.C. Defect and Additional Active Sites on the Basal Plane of Manganese-Doped Molybdenum Diselenide for Effective Enzyme Immobilization: In Vitro and in Vivo Real-Time Analyses of Hydrogen Peroxide Sensing. *ACS Appl. Mater. Interfaces* **2019**, *11*, 7862–7871. [[CrossRef](#)]
156. Ramaraj, S.; Sakthivel, M.; Chen, S.M.; Elshikh, M.S.; Chen, T.W.; Yu, M.C.; Ho, K.C. Electrochemical sensing of anti-inflammatory agent in paramedical sample based on FeMoSe<sub>2</sub> modified SPCE: Comparison of various preparation methods and morphological effects. *Anal. Chim. Acta* **2019**, *1083*, 88–100. [[CrossRef](#)] [[PubMed](#)]
157. Huang, K.J.; Liu, Y.J.; Zhang, J.Z.; Liu, Y.M. A novel aptamer sensor based on layered tungsten disulfide nanosheets and Au nanoparticles amplification for 17β-estradiol detection. *Anal. Methods* **2014**, *6*, 8011–8017. [[CrossRef](#)]
158. Huang, K.J.; Liu, Y.J.; Cao, J.T.; Wang, H.B. An aptamer electrochemical assay for sensitive detection of immunoglobulin e based on tungsten disulfide-graphene composites and gold nanoparticles. *RSC Adv.* **2014**, *4*, 36742–36748. [[CrossRef](#)]

159. Chou, S.S.; De, M.; Kim, J.; Byun, S.; Dykstra, C.; Yu, J.; Huang, J.; Dravid, V.P. Ligand conjugation of chemically exfoliated MoS<sub>2</sub>. *J. Am. Chem. Soc.* **2013**, *135*, 4584–4587. [[CrossRef](#)] [[PubMed](#)]
160. Wang, X.H.; Zheng, C.C.; Ning, J.Q. Influence of curvature strain and Van der Waals force on the inter-layer vibration mode of WS<sub>2</sub> nanotubes: A confocal micro-Raman spectroscopic study. *Sci. Rep.* **2016**, *6*, 33091. [[CrossRef](#)]
161. Mishra, A.; Pilloton, R.; Jain, S.; Roy, S.; Khanuja, M.; Mathur, A.; Narang, J. Paper-Based Electrodes Conjugated with Tungsten Disulfide Nanostructure and Aptamer for Impedimetric Detection of *Listeria monocytogenes*. *Biosensors* **2022**, *12*, 88. [[CrossRef](#)]
162. Della Pelle, F.; Rojas, D.; Silveri, F.; Ferraro, G.; Fratini, E.; Scroccarello, A.; Escarpa, A.; Compagnone, D. Class-selective voltammetric determination of hydroxycinnamic acids structural analogs using a WS<sub>2</sub>/catechin-capped AuNPs/carbon black-based nanocomposite sensor. *Microchim. Acta* **2020**, *187*, 296. [[CrossRef](#)]
163. Rojas, D.; Della Pelle, F.; Del Carlo, M.; Compagnone, D.; Escarpa, A. Group VI transition metal dichalcogenides as antifouling transducers for electrochemical oxidation of catechol-containing structures. *Electrochem. Commun.* **2020**, *115*, 106718. [[CrossRef](#)]
164. Della Pelle, F.; Vilela, D.; González, M.C.; Lo Sterzo, C.; Compagnone, D.; Del Carlo, M.; Escarpa, A. Antioxidant capacity index based on gold nanoparticles formation. Application to extra virgin olive oil samples. *Food Chem.* **2015**, *178*, 70–75. [[CrossRef](#)]
165. Della Pelle, F.; Scroccarello, A.; Sergi, M.; Mascini, M.; Del Carlo, M.; Compagnone, D. Simple and rapid silver nanoparticles based antioxidant capacity assays: Reactivity study for phenolic compounds. *Food Chem.* **2018**, *256*, 342–349. [[CrossRef](#)]
166. Govindasamy, M.; Wang, S.F.; Jothiramalingam, R.; Noora Ibrahim, S.; Al-lohedan, H.A. A screen-printed electrode modified with tungsten disulfide nanosheets for nanomolar detection of the arsenic drug roxarsone. *Microchim. Acta* **2019**, *186*, 420. [[CrossRef](#)] [[PubMed](#)]
167. Chen, T.W.; Rajaji, U.; Chen, S.M.; Chinnapaiyan, S.; Ramalingam, R.J. Facile synthesis of mesoporous WS<sub>2</sub> nanorods decorated N-doped RGO network modified electrode as portable electrochemical sensing platform for sensitive detection of toxic antibiotic in biological and pharmaceutical samples. *Ultrason. Sonochem.* **2019**, *56*, 430–436. [[CrossRef](#)] [[PubMed](#)]
168. Naguib, M.; Kurtoglu, M.; Presser, V.; Lu, J.; Niu, J.; Heon, M.; Hultman, L.; Gogotsi, Y.; Barsoum, M.W. Two-Dimensional Nanocrystals Produced by Exfoliation of Ti<sub>3</sub>AlC<sub>2</sub>. *Adv. Mater.* **2011**, *23*, 4248–4253. [[CrossRef](#)]
169. Zhang, J.; Kong, N.; Uzun, S.; Levitt, A.; Seyedin, S.; Lynch, P.A.; Qin, S.; Han, M.; Yang, W.; Liu, J.; et al. Scalable Manufacturing of Free-Standing, Strong Ti<sub>3</sub>C<sub>2</sub>T<sub>x</sub> MXene Films with Outstanding Conductivity. *Adv. Mater.* **2020**, *32*, 2001093. [[CrossRef](#)] [[PubMed](#)]
170. Huang, K.; Li, Z.; Lin, J.; Han, G.; Huang, P. Two-dimensional transition metal carbides and nitrides (MXenes) for biomedical applications. *Chem. Soc. Rev.* **2018**, *47*, 5109–5124. [[CrossRef](#)] [[PubMed](#)]
171. Ho, D.H.; Choi, Y.Y.; Jo, S.B.; Myoung, J.M.; Cho, J.H. Sensing with MXenes: Progress and Prospects. *Adv. Mater.* **2021**, *33*, 2005846. [[CrossRef](#)]
172. Gogotsi, Y.; Huang, Q. MXenes: Two-Dimensional Building Blocks for Future Materials and Devices. *ACS Nano* **2021**, *15*, 5775–5780. [[CrossRef](#)]
173. Tischer, W.; Wedekind, F. Immobilized Enzymes: Methods and Applications BT-Biocatalysis-From Discovery to Application. *Biocatal. Discov. Appl.* **1999**, *200*, 95–126.
174. Wu, B.; Li, Z.; Kang, Z.; Ma, C.; Song, H.; Lu, F.; Zhu, Z. An Enzymatic Biosensor for the Detection of D-2-Hydroxyglutaric Acid in Serum and Urine. *Biosensors* **2022**, *12*, 66. [[CrossRef](#)]
175. Liu, Y.; Zhang, X.; Tan, H.; Yan, Y.; Hameed, B.H. Effect of pretreatment by different organic solvents on esterification activity and conformation of immobilized *Pseudomonas cepacia* lipase. *Process Biochem.* **2010**, *45*, 1176–1180. [[CrossRef](#)]
176. Saleh, A.; Wustoni, S.; Bihar, E.; El-demellawi, J.K.; Zhang, Y.; Hama, A. Inkjet-printed Ti<sub>3</sub>C<sub>2</sub>T<sub>x</sub> MXene electrodes for multimodal cutaneous biosensing. *J. Phys. Mater.* **2020**, *3*, 044004. [[CrossRef](#)]
177. Zhang, Y.; Jiang, X.; Zhang, J.; Zhang, H.; Li, Y. Simultaneous voltammetric determination of acetaminophen and isoniazid using MXene modified screen-printed electrode. *Biosens. Bioelectron.* **2019**, *130*, 315–321. [[CrossRef](#)] [[PubMed](#)]
178. Liu, J.; Jiang, X.; Zhang, R.; Zhang, Y.; Wu, L.; Lu, W.; Li, J.; Li, Y.; Zhang, H. MXene-Enabled Electrochemical Microfluidic Biosensor: Applications toward Multicomponent Continuous Monitoring in Whole Blood. *Adv. Funct. Mater.* **2019**, *29*, 1807326. [[CrossRef](#)]
179. Zhang, J.; Sun, R.; Ruan, D.; Zhang, M.; Li, Y.; Zhang, K.; Cheng, F.; Wang, Z.; Wang, Z.M. Point defects in two-dimensional hexagonal boron nitride: A perspective. *J. Appl. Phys.* **2020**, *128*, 100902. [[CrossRef](#)]
180. Uosaki, K.; Elumalai, G.; Noguchi, H.; Masuda, T.; Lyalin, A.; Nakayama, A.; Taketsugu, T. Boron nitride nanosheet on gold as an electrocatalyst for oxygen reduction reaction: Theoretical suggestion and experimental proof. *J. Am. Chem. Soc.* **2014**, *136*, 6542–6545. [[CrossRef](#)] [[PubMed](#)]
181. Wang, Y.; Mayorga-Martinez, C.C.; Chia, X.; Sofer, Z.; Pumera, M. Nonconductive layered hexagonal boron nitride exfoliation by bipolar electrochemistry. *Nanoscale* **2018**, *10*, 7298–7303. [[CrossRef](#)] [[PubMed](#)]
182. Yue, Y.; Zeng, L.; Wang, X.; Su, L.; Sun, M.; Wu, B.; Yan, S. Loading of AgNPs onto the surface of boron nitride nanosheets for determination of scopoletin in *Atractylodes macrocephala*. *Sci. Rep.* **2019**, *9*, 3864. [[CrossRef](#)] [[PubMed](#)]
183. Öndeş, B.; Evli, S.; Uygün, M.; Aktaş Uygün, D. Boron nitride nanosheet modified label-free electrochemical immunosensor for cancer antigen 125 detection. *Biosens. Bioelectron.* **2021**, *191*, 113454. [[CrossRef](#)]
184. Lin, Y.; Williams, T.V.; Xu, T.B.; Cao, W.; Elsayed-Ali, H.E.; Connell, J.W. Aqueous dispersions of few-layered and monolayered hexagonal boron nitride nanosheets from sonication-assisted hydrolysis: Critical role of water. *J. Phys. Chem. C* **2011**, *115*, 2679–2685. [[CrossRef](#)]

185. Molazemhosseini, A.; Magagnin, L.; Vena, P.; Liu, C.C. Single-use disposable electrochemical label-free immunosensor for detection of glycated hemoglobin (HbA1c) using differential pulse voltammetry (DPV). *Sensors* **2016**, *16*, 1024. [[CrossRef](#)]
186. Torati, S.R.; Kasturi, K.C.S.B.; Lim, B.; Kim, C.G. Hierarchical gold nanostructures modified electrode for electrochemical detection of cancer antigen CA125. *Sens. Actuators B Chem.* **2017**, *243*, 64–71. [[CrossRef](#)]
187. Ma, H.; Sun, J.; Zhang, Y.; Bian, C.; Xia, S.; Zhen, T. Label-free immunosensor based on one-step electrodeposition of chitosan-gold nanoparticles biocompatible film on Au microelectrode for determination of aflatoxin B1 in maize. *Biosens. Bioelectron.* **2016**, *80*, 222–229. [[CrossRef](#)] [[PubMed](#)]
188. Liu, J.; Wang, J.; Wang, T.; Li, D.; Xi, F.; Wang, J.; Wang, E. Three-dimensional electrochemical immunosensor for sensitive detection of carcinoembryonic antigen based on monolithic and macroporous graphene foam. *Biosens. Bioelectron.* **2015**, *65*, 281–286. [[CrossRef](#)]
189. Qin, S.; Liu, D.; Wang, G.; Portehault, D.; Garvey, C.J.; Gogotsi, Y.; Lei, W.; Chen, Y. High and Stable Ionic Conductivity in 2D Nanofluidic Ion Channels Between Boron Nitride Layers. *J. Am. Chem. Soc.* **2017**, *139*, 6314–6320. [[CrossRef](#)]
190. Kokulnathan, T.; Vishnuraj, R.; Wang, T.J.; Kumar, E.A.; Pullithadathil, B. Heterostructured bismuth oxide/hexagonal-boron nitride nanocomposite: A disposable electrochemical sensor for detection of flutamide. *Ecotoxicol. Environ. Saf.* **2021**, *207*, 111276. [[CrossRef](#)] [[PubMed](#)]